COMPARISON OF TWO PHYSICAL OPTICS INTEGRATION APPROACHES FOR ELECTROMAGNETIC SCATTERING

A THESIS
SUBMITTED TO THE DEPARTMENT OF ELECTRICAL AND
ELECTRONICS ENGINEERING
AND THE INSTITUTE OF ENGINEERING AND SCIENCES
OF BILKENT UNIVERSITY
IN PARTIAL FULFILLMENT OF THE REQUIREMENTS
FOR THE DEGREE OF
MASTER OF SCIENCE

By
Ender Öztürk
September, 2008

I certify that I have read this thesis and that in my opinion it is fully adequate, in scope and in quality, as a thesis for the degree of Master of Science.

Prof. Dr. Ayhan Altıntaş (Supervisor)

I certify that I have read this thesis and that in my opinion it is fully adequate, in scope and in quality, as a thesis for the degree of Master of Science.

Prof. Dr. Hayrettin Köymen

I certify that I have read this thesis and that in my opinion it is fully adequate, in scope and in quality, as a thesis for the degree of Master of Science.

Prof. Dr. Birsen Saka

Approved for the Institute of Engineering and Sciences:

Prof. Dr. Mehmet Baray
Director of Institute of Engineering and Sciences

ABSTRACT

COMPARISON OF TWO PHYSICAL OPTICS INTEGRATION APPROACHES FOR ELECTROMAGNETIC SCATTERING

Ender Öztürk
M.S. in Electrical and Electronics Engineering
Supervisor: Prof. Dr. Ayhan Altıntaş
September, 2008

A computer program which uses two different Physical Optics (PO) approaches to calculate the Radar Cross Section (RCS) of perfectly conducting planar and spherical structures is developed. Comparison of these approaches is aimed in general by means of accuracy and efficiency. Given the certain geometry, it is first meshed using planar triangles. Then this imaginary surface is illuminated by a plane wave. After meshing, Physical Optics (PO) surface integral is numerically evaluated over the whole illuminated surface. Surface geometry and ratio between dimension of a facet and operating wavelength play a significant role in calculations. Simulations for planar and spherical structures modeled by planar triangles have been made in order to make a good comparison between the approaches. Method of Moments (MoM) solution is added in order to establish the accuracy. Backscattering and bistatic scattering scenarios are considered in simulations. The effect of polarization of incident wave is also investigated for some geometry. Main difference between approaches is in calculation of phase differences. By this study, a comprehensive idea about accuracy and usability due to computation cost is composed for different PO techniques through simulations under different circumstances such as different geometries (planar and curved), different initial polarizations, and different electromagnetic size of facets.

Keywords: Physical Optics (PO), Triangular Surface Meshing, Radar Cross Section (RCS), Method of Moments (MoM).

ÖZET

İKI FİZİKSEL OPTİK İNTEGRALİ YAKLAŞIMININ ELEKTROMANYETİK SAÇINIM AÇISINDAN KARŞILAŞTIRILMASI

Ender Öztürk
Elektrik ve Elektronik Mühendisliği Bölümü Yüksek Lisans
Tez Yöneticisi: Prof. Dr. Ayhan Altıntaş
Eylül, 2008

İki farklı Fiziksel Optik metodu kullanarak düzlemsel ve küresel yüzeylerin Radar Kesit Alanlarını hesaplayan bir bilgisayar programı geliştirilmiştir. Genel itibariyle farklı ilk şartlar için bu metodların doğruluk ve verimliliğinin karşılaştırılması amaçlanmıştır. Verilen düzlemsel ve küresel yüzey öncelikle üçgenleme metodu kullanılarak düzlemlere bölünmüştür. Üçgenlemenin ardından bu düzlemler kullanılarak iki farklı metod ile Fiziksel Optik yüzey integrali nümerik olarak hesaplanmıştır. Kullanılan üçgenlerin elektromanyetik büyüklüğü ve yüzeyin geometrisi sonuçlar üzerinde kayda değer etkiler oluşturmaktadır. İki metod arasında iyi bir karşılaştırma yapabilmek için pek çok simülasyon yapılmıştır. Literatürden edinilen Momentler Yöntemi sonucu da gerçeğe en yakın sonucun da değerlendirmesini yapabilmek için Fiziksel Optik sonuçlarıyla birlikte kullanılmıştır. Gelen dalganın polarizasyonu ile tam iletken olmayan yüzey özelliklerinin saçılan dalga üzerine etkisi de küresel yüzeyler için incelenmiıtir. İki metod arasındaki fark bir üçgen içindeki faz farkının hesaplanışındadır. Bu çalışma ile, iki farklı Fiziksel Optik tekniği arasında farklı yüzey geometrileri (düzlemsel ve küresel), farklı uyarım polarizasyonları ve farklı elektromanyetik üçgenleme büyüklüklükleri için kapsamlı bir fikir oluşturulmuştur.

Anahtar Kelimeler: Fiziksel Optik, yüzey üçgenleme, Radar Kesit Alanı, Momentler Yöntemi.

ACKNOWLEDGMENTS

I would like to thank my supervisor Prof. Ayhan Altıntaş for his invaluable help, encouragement and motivation during my MS studies. I would also like to thank Dr. Hayrettin Köymen and Dr. Birsen Saka for accepting to be in the thesis committee and commenting on the thesis. Finally, I would gladly like to appreciate my beloved wife for her priceless help and belief.

Contents

List of Figures

To my family...

Chapter 1

INTRODUCTION

When a conducting body is illuminated by an electromagnetic wave, electric currents are induced on the surface of the body. This induction behaves in accordance with Maxwell's equations and related electromagnetic boundary conditions. These induced currents act as secondary sources and produce an electromagnetic field which is called *the scattered field* and is a function of the operating frequency, the polarization of the incident wave and the shape of the scatterer.

The spatial distribution of scattered power density in a certain observation direction may be expressed by a fictitious cross sectional area called Radar Cross Section (RCS) which is a function of the shape of the body and the polarization of incident plane wave. This certain direction is the direction of incident wave in the backscattering case. RCS is the area through which the flux of the incident power density would yield the scattered power density isotropically. There are three RCS regimes that characterize the relationship between the wavelength and the body size: High Frequency (HF) scattering, resonant scattering and Low Frequency (LF) scattering.

In the high frequency regime, there are various techniques for calculating scattered field and/or RCS. Physical Optics (PO) and Geometrical Optics (GO) are the two main ones. GO is based on the classical ray-tracing of incident, reflected and transmitted rays. PO is based on the integration of induced currents predicted by GO.

For the GO, RCS is a function of radius of curvature at the specular point, even in bistatic scattering directions. Specular point may be described as the intersection point of the shortest path between the incident and observation point and the scatterer in the existence of reflection. Bistatic scattering means, separate incident and observation directions. However, this approach may fail if the surface is flat, since result of the GO blows up for plane wave incidence because there are infinite number of reflected rays due to the facet that the radius of curvature is infinite. PO surface integral method, on the other hand, gives quite fine results around the specular direction [1] even for flat surfaces, however may fail at wide angles from the specular direction. It is noted that, GO does not contain diffracted rays and PO diffraction is not accurate. However, as the frequency is increased, the contribution of diffraction gets smaller. Detailed information about these techniques may be found in [2] and [3]. Throughout this thesis, only PO is studied to calculate total scattered field.

In this study, the scattering objects are meshed using triangular plates. This type of meshing is called *triangulation*, and each piece of triangles is called a single *facet*. Then for each facet, PO scattered field is computed with two different PO techniques. Adding up field contributions of each facet, total scattered field is calculated.

For the first approach, introduced in [1], analytical solution of PO radiation integral for finite flat surfaces is used in calculating field contribution of a single facet. Since the radiation integral is taken analytically, phase differences within a facet is taken into account in a precise manner. Induced surface currents are calculated at each point of a facet and integrated along all points on the mesh.

For the second approach, introduced in [4], both induced surface currents and field produced by this currents are calculated as if there is no phase difference between any points within a facet. Midpoint of the facet is taken as the reference point, and, fictitiously, all the area is assumed to be at that point. By this approximation, instead of taking the integral analytically, a summation of each mesh contributions is performed for computing total scattered field. Therefore, a significant amount of computational simplicity is gained in trade-off of the accuracy of the solution.

A computer program is developed in MATLAB for Radar Cross Section and scattered field calculations. The calculations are done for some simple shaped targets as flat plates, PEC spheres and ellipsoids for different polarizations of initial excitation and various meshing densities. Solutions are compared with the ones in the literature.

Chapter 2

THEORY

Physical Optics is used in this thesis for calculating RCS of targets having conducting surfaces. When a surface is illuminated by a wave, surface currents are induced. PO calculates the scattered field by integrating this currents over the whole surface. In order to compute the total field, the surface should be pulled into pieces. In the implementation, surfaces are represented by small planer triangular facets. Higher the number of facets, better representation of the surface especially for curved surfaces. Afterwards, scattered field is computed for each facet and summed up in order to get total field scattered from the body.

In this procedure, there are certain factors which affect the computational cost and complexity. First of all, computational cost directly depends on the number of facets. High quality of representation of the body necessitates large number of facets which boosts up the computation time and allocated memory size during computation. The results presented here conforms with the PO results in the literature, [5] and [6].

Two different techniques for evaluation of PO surface integral is introduced in the following sections:

2.1 Physical Optics Integral Derivation

Physical Optics follows the following steps in order to find the scattered field, as also explained in [7]:

1. Electric and magnetic currents are induced on the illuminated facets and these currents are found by Geometrical Optics. For Perfect Electric Conductors (PECs), total field is the sum of fields due to incident and reflected rays.

2. An induced surface current is then a function of the tangential component of the incident wave. Since GO rays exist only on the illuminated facets, PO currents for conducting body is given by:

$$\vec{J}_s = \begin{cases} 2\hat{n} \times \vec{H}^i, & \text{Illuminated region} \\ 0, & \text{Shadow region} \end{cases} \tag{2.1}$$

3. Using the radiation integral, the surface current is integrated over the surface.

4. Total field on the surface of a facet is the sum of incident and the reflected field, which may be expressed with the equations below:

$$\vec{E}^t = \vec{E}^i + \vec{E}^s, \tag{2.2}$$

$$\vec{H}^t = \vec{H}^i + \vec{H}^s. \tag{2.3}$$

Assuming the excitation source is far enough; incident wave is taken as a plane wave and may be expressed as follows:

$$\vec{E}^i = \vec{E}_0^i e^{-jk\hat{k}_i.\vec{r}}, \tag{2.4}$$

$$\vec{H}^i = \vec{H}_0^i e^{-jk\hat{k}_i.\vec{r}}. \tag{2.5}$$

Relation between real and constant amplitude vectors E_0 and H_0 is given for plane waves as:

$$\vec{H}_0^i = \frac{1}{\eta}\hat{k}_i \times \vec{E}_0^i, \tag{2.6}$$

where η is the intrinsic impedance of free space, the wavenumber $k = w\sqrt{\epsilon\mu}$ and $\hat{k}_i$ is the unit vector along the propagation vector of incident wave and is given as:

$$\hat{k}_i = -(\hat{x}\sin\theta^i\cos\phi^i + \hat{y}\sin\theta^i\sin\phi^i + \hat{z}\cos\theta^i). \tag{2.7}$$

The incident electric field is written in terms of its orthogonal components in spherical coordinates as:

$$\vec{E}^i = (\vec{E}_\theta^i\hat{\theta}^i + \vec{E}_\phi^i\hat{\phi}^i)e^{-jk\hat{k}_i.\vec{r}}, \tag{2.8}$$

where (θ^i, ϕ^i) are the spherical coordinates of the source and $(\hat{r}^i, \hat{\theta}^i, \hat{\phi}^i)$ are the unit vectors. The incident magnetic field is given by:

$$\begin{aligned} \vec{H}_0^i &= \frac{1}{\eta}\hat{k}_i \times \vec{E}_0^i && (2.9) \\ &= \frac{1}{\eta}(-E_\phi^i\hat{\theta}^i + E_\theta^i\hat{\phi}^i)e^{-jk\hat{k}_i.\vec{r}}. && (2.10) \end{aligned}$$

Magnetic vector potential is a useful tool in order to calculate field components. This vector potential of the scattered field at $\vec{r}_s$ is proportional to the surface integral of induced current and is given by:

$$\vec{A}^s = \frac{\mu}{4\pi r_s} e^{-jkr_s} \int_S \int \vec{J} e^{jkr_s.\vec{r}} ds. \tag{2.11}$$

Using $-jwt$ time convention, relation between vector potential and electric field is given as $\vec{E}_s = -jw\vec{A}^s$. And applying far field approximation, electric field expression turns out be:

$$\vec{E}^s = \frac{jw\mu}{2\pi r_s} e^{-jkr_s} \int_S \int \hat{n} \times \vec{H}^i e^{-jk\hat{k}_s.\vec{r}} ds. \tag{2.12}$$

Using equations (2.9) and (2.12), the final scattered field is found evaluating the following equation which is called PO surface integral:

$$\vec{E}^s = \frac{e^{jkr_s}}{r_s} (\vec{E}^i_\phi \hat{\theta}^i - \vec{E}^i_\theta \hat{\phi}^i) \times (\frac{j}{\lambda}) \int_S \int \hat{n} e^{jk(\hat{r}_i + \hat{r}_s).\vec{r}} ds. \tag{2.13}$$

2.2 Triangular Meshing

In this study, the target surface is meshed into triangular flat facets, in order to calculate PO surface integral. To represent these facets, first the whole body is modeled by enough number of points corresponding to mesh corners. Afterwards, these points are connected in such a way that Cartesian coordinates of corner points, midpoint coordinates and the area of each triangle are kept in a main array of meshing. Meshing process for flat surfaces is explained below:

1. Assuming that, the plate is lying on the $x-y$ plane, two arrays are created whose elements taking values linearly between $[-0.5, 0.5]$ with sizes equal to each other depending on how many facets is desired. These arrays represent the x and y coordinates of corners of triangles.

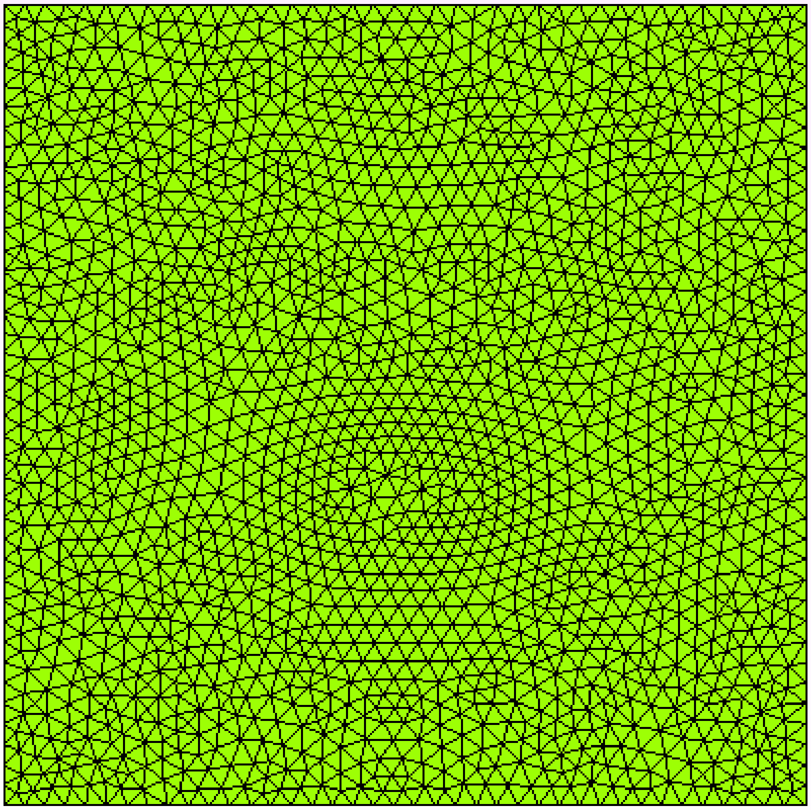

Figure 2.1: Representation of a plate using triangular facets

2. Let the size of the array be $N + 1$, this means there exists N^2 rectangles on the plate. Therefore, area of a single triangle is constant and found as: Area $= \frac{1}{2N^2}$
3. A third main array is created to hold three coordinates of corners of each right triangle and midpoint's coordinates which are derived from corners.

Modeling accuracy is not an issue for flat plates since facets are planar also. Figure (2.1) is an example for a meshed square plate. However, for curved surfaces, using flat triangles may cause modeling problems which is inevitable since infinite number of pieces is needed to perfectly represent a curved surface, such as a sphere, exactly. On the other hand, increasing the number of facets is expected to give better results. In this study, only spherical geometries are used as curved surfaces. In figure (2.2), a meshed sphere is shown. Meshing procedure for spherical geometries has common points but also different issues:

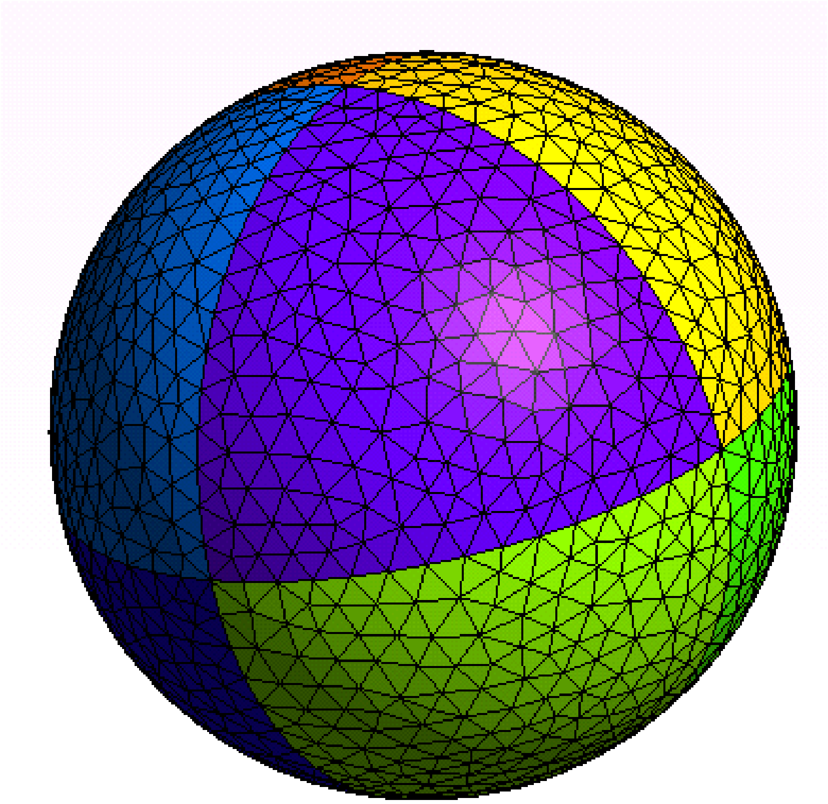

Figure 2.2: Approximation of a sphere using triangular facets

1. The procedure begins with slicing the body into N parallel planes orthogonal to the z axis. N should be an even number in order to save the symmetry and to avoid singularities. (See figure (2.3)) These planes are expressed as: $z = z_n(n = 1, 2, ...N)$ This intervals between slices are determined due to constant intervals between elevation angles principle.

$$\theta_n = \frac{n\pi}{N} \tag{2.14}$$

$$\begin{aligned} \delta z_n(n) &= R(\cos(\theta_n) - \cos(\theta_{n-1})) && (2.15) \\ &= R(\cos(\frac{n\pi}{N}) - \cos(\frac{(n-1)\pi}{N})) && (2.16) \\ &= -2R(\sin(\frac{(2n-1)\pi}{2N})\sin(\frac{\pi}{2N})) && (2.17) \end{aligned}$$

.

2. Intersection points of a plane and the body is a circle for each plane. These circles are represented by another array holding x and y coordinates

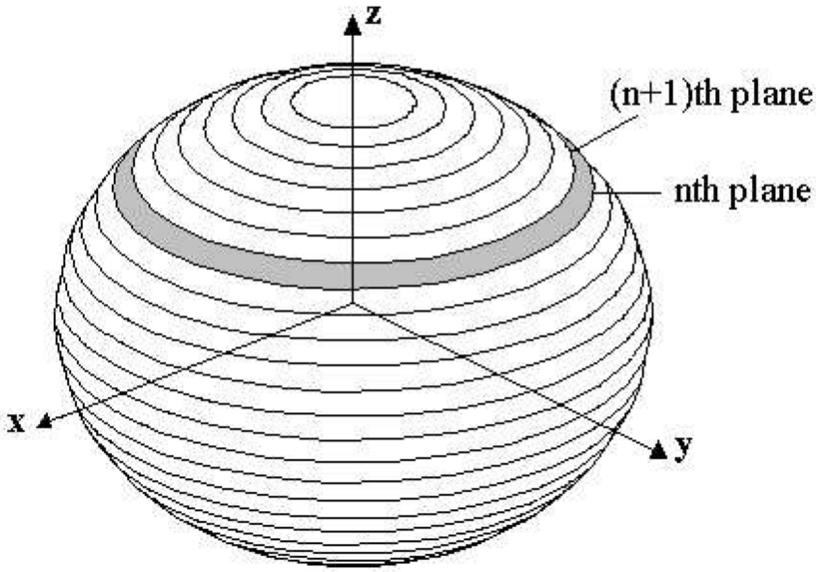

Figure 2.3: Contouring the target by splitting along the z-axis

of points. Therefore with a total number of $\sum_{n=0}^{N}\sum_{m=0}^{M(n)}, (x_{mn}, y_{mn}, z_n)$ points, the spherical surface is modeled.

3. At the next step, there assumed N pieces of longitudes on the sphere. Intersection points of these longitudes and horizontally placed circles are all kept in a main array in order to determine parameters of triangular facets. In figure (2.4) perpendicular lines are seen. Intermediate regions between z_n^{th} and $z_{(n+1)}^{th}$ planes and longitudes L_m and L_{m+1} are separated into two triangular pieces. Three points represent a triangle, corners of the triangle, and all other parameters are derived from these points. Let $P_{z_nL_m}(x, y, z)$ be a point on the sphere and also the intersection point of z_n^{th} plane and L_m^{th} longitude. Then, three points, $P_{z_nL_m}$, $P_{z_{n+1}L_m}$ and $P_{z_nL_{m+1}}$ represent the first triangle. $P_{z_{n+1}L_m}$, $P_{z_{n+1}L_{m+1}}$ and $P_{z_{n+1}L_m}$ represent the second triangle. All three coordinates of all intersection points are known.

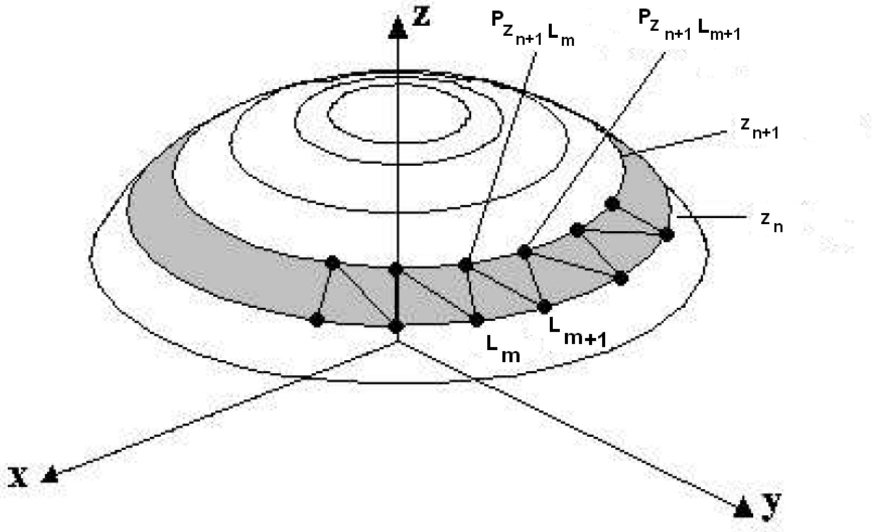

Figure 2.4: Triangular facets on the surface of a sphere

4. Since corners of the triangles are known, its area is calculated using its circumference. Let a, b and c be the lengths of the edges of the facet:

$$\text{Area} = \sqrt{u(u-a)(u-b)(u-c)} \quad \text{where } u = \frac{(a+b+c)}{2}. \tag{2.18}$$

5. Midpoint of the triangle is calculated using the coordinates of corner points. One thirds of sum of x coordinates of corners give x coordinate of midpoint, and this procedure is applied for y and z.

$$X_{\text{mid}} = P_{1^{st}Corner}(x) + P_{2^{nd}Corner}(x) + P_{3^{rd}Corner}(x), \tag{2.19}$$

$$Y_{\text{mid}} = P_{1^{st}Corner}(y) + P_{2^{nd}Corner}(y) + P_{3^{rd}Corner}(y), \tag{2.20}$$

$$Z_{\text{mid}} = P_{1^{st}Corner}(z) + P_{2^{nd}Corner}(z) + P_{3^{rd}Corner}(z). \tag{2.21}$$

6. Determination of normal vector for each of the facets is an important issue. It should direct outward to the surface, since all the formulations are derived with this assumption. Regarding a unit sphere centered at the origin of the coordinate system, it is easy to determine the x, y and z components of $\hat{n}_{mn}$. Under these conditions, coordinates of midpoint, $(x, y, z)_{midpoint}$, of a facet is the same as components of normal vector for that facet.

Through these steps, three coordinates of three corners of facets are hold in addition to the area and coordinates of midpoint of triangles. For planar surfaces, normal vector is constant and in $+z$ direction for the moment.

2.3 Coordinate Transformation

Before calculating the surface integral, some sort of coordinate transformation is needed. Each facet is assumed to stand on a local Cartesian coordinate system, (x_l, y_l, z_l) so that all facets lie on $x_l - y_l$ plane in calculations. In order to achieve the transformation, unit vectors for the local coordinates should be defined. Let $\vec{e}_1$, $\vec{e}_2$ and $\vec{e}_3$ be the edges of the triange in global coordinates. As a starting point, $\vec{e}_3$ may be taken along y_l, and one corner of the triangle coincide with the origin. Then the unit vectors of local system are given by:

$$\hat{y}_l = -\frac{\vec{e}_3}{|\vec{e}_3|}, \tag{2.22}$$

$$\hat{z}_l = -\frac{\vec{e}_1 \times (-\vec{e}_3)}{|\vec{e}_1 \times \vec{e}_3|}, \tag{2.23}$$

$$\hat{x}_l = \hat{y}_l \times \hat{z}_l. \tag{2.24}$$

Local and global coordinate systems are seen on Figure (2.5) for a single facet. Global coordinates are represented by (x_g, y_g, z_g). In addition, a new parameter is introduced here, $\vec{c}_l$, which is the distance vector between the origins of two

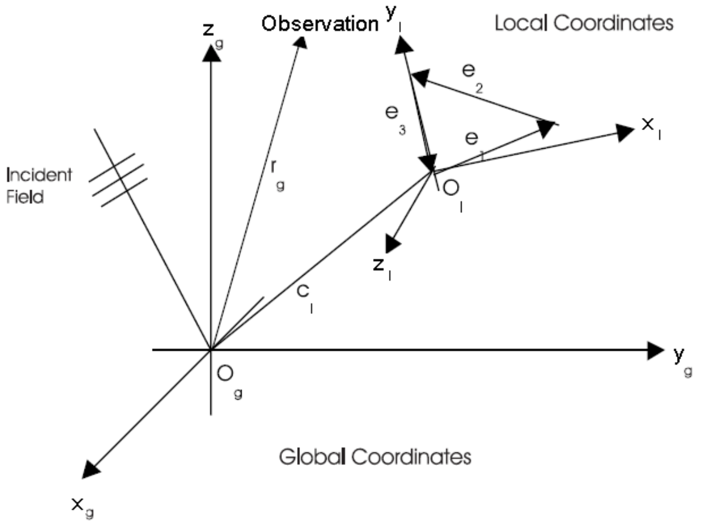

Figure 2.5: Local coordinates of a triangle residing in global coordinates

coordinate systems, local and global. Also it is noted that, $\vec{r_g}$ is the position vector defined in global coordinates.

First thing to do is to transform incident wave given in rectangular coordinates into local coordinate system. A transform matrix is used for this purpose. Expression of this matrix $\overline{\overline{m}}_1$ is given as:

$$\overline{\overline{m}}_1 = \begin{pmatrix} \hat{x}_g.\hat{x}_l & \hat{x}_g.\hat{y}_l & \hat{x}_g.\hat{z}_l \\ \hat{y}_g.\hat{x}_l & \hat{y}_g.\hat{y}_l & \hat{y}_g.\hat{z}_l \\ \hat{z}_g.\hat{x}_l & \hat{z}_g.\hat{y}_l & \hat{z}_g.\hat{z}_l \end{pmatrix}. \tag{2.25}$$

Therefore, initial field in local coordinates may be written in terms of global coordinates as below:

$$\begin{pmatrix} E^i_{xl} \\ E^i_{yl} \\ E^i_{yl} \end{pmatrix} = \overline{\overline{m}}_1 \cdot \begin{pmatrix} E^i_{xg} \\ E^i_{yg} \\ E^i_{yg} \end{pmatrix}. \tag{2.26}$$

Second thing is to write the incident field in local spherical coordinate system. Another transform matrix is used which is called $\overline{\overline{m}}_2$ and given as:

$$\overline{\overline{m}}_2 = \begin{pmatrix} \hat{x}_l.\hat{\theta}_l & \hat{x}_l.\hat{\phi}_l \\ \hat{y}_l.\hat{\theta}_l & \hat{y}_l.\hat{\phi}_l \\ \hat{z}_l.\hat{\theta}_l & \hat{z}_l.\hat{\phi}_l \end{pmatrix}. \tag{2.27}$$

By applying this transformation, incident field in local spherical coordinate system is found by

$$\begin{pmatrix} E^i_{\theta l} \\ E^i_{\phi l} \end{pmatrix} = \overline{\overline{m}}_2 \cdot \begin{pmatrix} E^i_{xl} \\ E^i_{yl} \\ E^i_{zl} \end{pmatrix}. \tag{2.28}$$

The matrix $\overline{\overline{m}}_2$ may be written in terms of sines and cosines. This form is more useful for calculations.

$$\overline{\overline{m}}_2 = \begin{pmatrix} \cos\theta_l \cos\phi_l & -\sin\phi_l \\ \cos\theta_l \sin\phi_l & \cos\phi_l \\ -\sin\theta_l & 0 \end{pmatrix}, \tag{2.29}$$

where θ_l and ϕ_l are azimuth and elevation angles in local coordinates. These angles may be found from the propagation vector, $\hat{k}_i$.

Since the matrices $\overline{\overline{m}}_1$ and $\overline{\overline{m}}_2$ are unitary transformation matrices, transposes of these matrices may be used for the inverse transformation. Transpose of $\overline{\overline{m}}_1$

converts local coordinates into global coordinates. Similarly, transpose of $\overline{\overline{m}}_2$ converts spherical coordinates into rectangular.

In addition to these, another matrix, $\overline{\overline{m}}_2^G$ shall be used in the calculations. This matrix transforms the scattered field from rectangular coordinates into spherical coordinates in global system:

$$\overline{\overline{m}}_2^G = \begin{pmatrix} \hat{x}_g.\hat{\theta}_g & \hat{x}_g.\hat{\phi}_g \\ \hat{y}_g.\hat{\theta}_g & \hat{y}_g.\hat{\phi}_g \\ \hat{z}_g.\hat{\theta}_g & \hat{z}_g.\hat{\phi}_g \end{pmatrix} = \begin{pmatrix} \cos\theta_g^s \cos\phi_g^s & -\sin\phi_g^s \\ \cos\theta_g^s \sin\phi_g^s & \cos\phi_g^s \\ -\sin\theta_g^s & 0 \end{pmatrix}. \tag{2.30}$$

Mainly there exist two kinds of transformation matrix which are rectangular-to-spherical and global-to-local transformation matrices. By arranging the parameters and taking transposes, all the transformation matrices required in calculations may be derived.

2.4 Implementation of Approach 1

The incident electric field in local coordinates is given by

$$\vec{E}_l^i = (E_{\theta l}^i \hat{\theta}_l^i + E_{\phi l}^i \hat{\phi}_l^i) e^{j\vec{k}^i.\vec{r}_l}. \tag{2.31}$$

Implementation of Physical Optics is described in section 2.1. The θ and ϕ components of scattered field as given in equation (2.13) may be written shortly in local coordinates and in terms of surface currents as:

$$E_{\theta l}^s(x_l, y_l) = \frac{-jw\mu}{4\pi r} e^{jkr_i} \int_S \int (J_{xl}\cos\theta\cos\phi + J_{yl}\cos\theta\sin\phi - J_{zl}\sin\theta) e^{jkh} ds', \tag{2.32}$$

$$E^s_{\phi l}(x_l, y_l) = \frac{-jw\mu}{4\pi r} e^{jkr_i} \int_S \int (J_{xl} \sin\phi + J_{yl} \cos\phi) e^{jkh} ds', \tag{2.33}$$

where $h = x'_l \sin\theta \cos\phi + y'_l \sin\theta \sin\phi + z'_l \cos\theta$. S in the integral limit stands for the surface of planar surface of each facet.

Distance from the origin of local coordinate system, $\vec{r_l}$ may be written in terms of known parameters. Using far field approximation, $\vec{r_l}$ turns out to be:

$$\vec{r_l} = \vec{r}_g - (\hat{k}_s.\vec{c_l})\vec{c_l}, \tag{2.34}$$

where $\hat{k}_s$ is the propagation vector of scattered field and $\vec{c_l}$ is the distance vector between origins of global and local coordinate systems pointing local system's origin. The equations (2.32) and (2.33) may be written in matrix form:

$$\begin{pmatrix} E^s_{\theta l}(r,\theta,\phi) \\ E^s_{\phi l}(r,\theta,\phi) \end{pmatrix} = \begin{pmatrix} E^i_{\theta l} \\ E^i_{\phi l} \end{pmatrix} \overline{\overline{F}} I_0 \frac{jw\mu}{2\pi r} e^{jkr}. \tag{2.35}$$

The matrix $\overline{\overline{F}}$ is the Physical Optics scattering function defined in local coordinates. Its explicit form is as follows:

$$\overline{\overline{F}} = \begin{pmatrix} -\cos\theta^s \cos(\phi^s - \phi^i) & \sin(\phi^s - \phi^i) \\ -\cos\theta^s \cos\theta^i \sin(\phi^s - \phi^i) & -\cos\theta^i \cos(\phi^s - \phi^i) \end{pmatrix}. \tag{2.36}$$

The difference between two approaches, phase factor, is taken into account in this approach by the integral I_0 which is given by

$$I_0 = \int_{x'_l=a}^{b} \int_{y'_l=\alpha(x'_l)}^{\beta(x'_l)} e^{j(ux'_l+vy'_l)} dx'dy', \tag{2.37}$$

where the unknown terms used in the equation are:

$$u = k(\sin\theta^i \cos\phi^i + \sin\theta^s \cos\phi^s), \tag{2.38}$$

$$v = k(\sin\theta^i \sin\phi^i + \sin\theta^s \sin\phi^s), \tag{2.39}$$

the terms in the limits of the integral equation are described in figure (2.6) They may be expressed as:

$$\alpha(x'_l) = \alpha_0 + \alpha_1 x'_l, \tag{2.40}$$

$$\beta(x'_l) = \beta_0 + \beta_1 x'_l. \tag{2.41}$$

Considering these equations above, the equation (2.37) may be rewritten as:

$$I_0 = \frac{1}{jv}(e^{jv\beta_0}\frac{e^{jb(u+v\beta_1)} - e^{ja(u+j\beta_1)}}{j(u+v\beta_1)} - e^{jv\alpha_0}\frac{e^{jb(u+v\alpha_1)} - e^{ja(u+j\alpha_1)}}{j(u+v\alpha_1)}). \tag{2.42}$$

As a result using all the derivations done up to this point, a closed form expression for the scattered field may be defined:

$$E^s(\theta_g, \phi_g) = K\overline{\overline{m}}_2(\theta_g, \phi_g) \cdot \overline{\overline{m}}_1^T \cdot \overline{\overline{m}}_2^T(\theta_l^s, \phi_l^s) \cdot \overline{\overline{F}} \cdot \overline{\overline{m}}_2(\theta_l^i, \phi_l^i) \cdot \overline{\overline{m}}_1 \cdot \vec{E}^i(0). \tag{2.43}$$

At the left hand side of the equation there exists only one term. $E^s(\theta_g, \phi_g)$ is the far field scattered electric field in global coordinates directed to a spherical direction represented by the angles θ_g and ϕ_g. On the right hand side, first term is K, which is a complex constant including phase difference between local and global coordinate systems:

$$K = I_0 \frac{jw\mu}{2\pi r} e^{-jk(r - \hat{k}^i \cdot \vec{c}_l - \hat{k}^s \cdot \vec{c}_l)}. \tag{2.44}$$

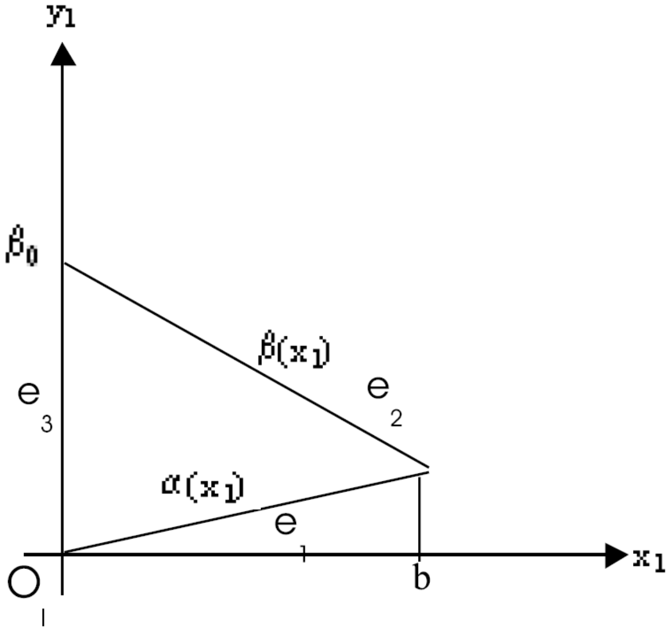

Figure 2.6: The triangle in local coordinates

The second term, $\vec{E}^i(0)$, is the initial field vector in global coordinates expressed rectangular system. The next term, $\overline{\overline{m}}_1$, converts the incident field into local rectangular coordinate system. Following term, $\overline{\overline{m}}_2(\theta_l^i, \phi_l^i)$ stands for converting rectangular into spherical in local coordinates. The matrix, $\overline{\overline{F}}$, as mentioned before, is the Physical Optics scattering matrix. At this point, scattered field in local spherical coordinates for a single facet is obtained. Then, $\overline{\overline{m}}_2^T(\theta_l^s, \phi_l^s)$ converts scattered field into Cartesian coordinates in local system. $\overline{\overline{m}}_1^T$ works for converting scattered field in local to global coordinate system in Cartesian. Finally the last term, $\overline{\overline{m}}_2(\theta_g, \phi_g)$ expresses scattered field in spherical coordinates.

Extending this solution to the whole surface, each scattered field from each facet should be summed up in order to find total scattered field. Then, the total field is used to calculate Radar Cross Section of scatterers. Polarization included expressions for RCS are as follows:

$$\sigma_{\theta\theta} = \lim_{r\to\infty} 4\pi r^2 \frac{|\vec{E}^s_\theta|^2}{|\vec{E}^i_\theta|^2}, \tag{2.45}$$

$$\sigma_{\phi\phi} = \lim_{r\to\infty} 4\pi r^2 \frac{|\vec{E}^s_\phi|^2}{|\vec{E}^i_\phi|^2}, \tag{2.46}$$

$$\sigma_{\theta\phi} = \lim_{r\to\infty} 4\pi r^2 \frac{|\vec{E}^s_\theta|^2}{|\vec{E}^i_\phi|^2}, \tag{2.47}$$

$$\sigma_{\phi\theta} = \lim_{r\to\infty} 4\pi r^2 \frac{|\vec{E}^s_\phi|^2}{|\vec{E}^i_\theta|^2}. \tag{2.48}$$

Radar Cross Section (RCS) is a characteristic property of the scattering body and actually a measure of the power that is returned or scattered in a given direction, normalized with respect to the power density of the incident field. It is defined in [8] as *the area required to be cut out of the incident wavefront, at the position of the scatterer, so the power thereby intercepted would, if radiated isotropically, create the same power density at the observation point as does the scatterer itself.* RCS should be independent from distance of observation point. This is done by the multiplication factor $4\pi r^2$. Including polarization information of both incident and scattered waves, four possible RCS definitions are given above. It can be concluded that, RCS is a function of the shape of the target, operation frequency, incident and observation polarizations.

2.5 Implementation of Approach 2

This approach is easier to implement with respect to previous approach. Implementation may be continued from the equation (2.13) derived in section 2.1:

$$\vec{E}^s = \frac{e^{jkr_s}}{r_s}(E^i_\phi \hat{\theta}^i - E^i_\theta \hat{\phi}^i) \times (\frac{j}{\lambda}) \int_S \int \hat{n} e^{jk(\hat{r}_i + \hat{r}_s).\vec{r}} ds. \tag{2.49}$$

In order to calculate this equation, a new vector quantity should be introduced here as:

$$\vec{S} = (\frac{j}{\lambda}) \int \int \hat{n} e^{jk(\hat{r}_i + \hat{r}_s) \cdot \vec{r}} ds, \tag{2.50}$$

the scattered field may also be written as in its orthogonal components

$$\vec{E}_s = (E^s_\theta \hat{\theta}_s + E^s_\phi \hat{\phi}_s) \frac{e^{-jkr_s}}{r_s}. \tag{2.51}$$

Using (2.13), (2.50), (2.51) and the vector identity given below,

$$\vec{A} \cdot (\vec{B} \times \vec{C}) = (\vec{A} \times \vec{B}) \cdot \vec{C}, \tag{2.52}$$

scattered field expressions are found as:

$$\vec{E}^s_\theta = (E^i_\theta \hat{\phi}_i \times \hat{\theta}_s + E^i_\phi \hat{\theta}_s \times \hat{\theta}_i) \cdot \vec{S}, \tag{2.53}$$

$$\vec{E}^s_\phi = (E^i_\theta \hat{\phi}_i \times \hat{\phi}_s + E^i_\phi \hat{\phi}_s \times \hat{\theta}_i) \cdot \vec{S}. \tag{2.54}$$

These two equations can be combined and expressed in matrix form as:

$$\begin{pmatrix} E^s_\theta \\ E^s_\phi \end{pmatrix} = \begin{pmatrix} (\hat{\phi}^i \times \hat{\theta}^s) \cdot \vec{S} & (\hat{\theta}^s \times \hat{\theta}^i) \cdot \vec{S} \\ (\hat{\phi}^i \times \hat{\phi}^s) \cdot \vec{S} & (\hat{\phi}^s \times \hat{\theta}^i) \cdot \vec{S} \end{pmatrix} \begin{pmatrix} E^i_\theta \\ E^i_\phi \end{pmatrix}. \tag{2.55}$$

The 2 by 2 matrix in the previous equation is the *scattering matrix* which binds the scattered field to incident field component by component. In order to calculate this matrix, (2.50) should be found first. Since (2.50) is a surface integral, $\vec{S}$ can be calculated by superposing the contributions of each facet. The difference between this approach and the previous one, contribution of a single triangle, is written as:

$$\vec{S}_t = (\frac{j}{\lambda}) \hat{n}_t e^{jk(\hat{r}_i + \hat{r}_s) \cdot \vec{r}_t} \Delta s_t \text{ for } t = 1 : C, \tag{2.56}$$

where C is the total number of illuminated facets on the surface of the scatterer and Δs_t is the area of t^{th} triangle. Therefore, $\vec{S}$ can be expressed as a sum:

$$\vec{S} = (\frac{j}{\lambda}) \sum_{t=0}^{C} \hat{n}_t e^{jk(\hat{r}_i + \hat{r}_s)\cdot\vec{r}_t} \Delta s_t. \tag{2.57}$$

Note that only illuminated facets make contribution to the sum in calculating $\vec{S}$. Therefore, in order to define whether a facet is illuminated or not, a new parameter is introduced:

$$I_t = \hat{n}_t \cdot \hat{r}_i. \tag{2.58}$$

If I_t is less then 0, this means that facet is in shadow region. If else, it is in illuminated region. Simulations and comparisons of these two approaches are done in the next chapter.

The scattering matrix for the targets which have axial symmetry with respect to z-axis, closed form expressions for (2.50) can be derived. The results in [9] well-agrees with the ones calculated in here.

Chapter 3

APPLICATIONS

For RCS and scattered power computations, a computer program is written in MATLAB. The program includes mesh generation code for plate and spherical geometries. In order to stay in high frequency region, size of the scatterer should be electrically large, namely large with respect to the wavelength. To implement PO integration, targets are generally divided into much smaller pieces and integration over each piece is superposed. Comparisons of the two PO integration methods are made in this chapter using numerical simulations.

To represent an arbitrary surface with flat plates, edges of the facets should be small, preferably less than or equal to $\frac{\lambda}{10}$. Smaller values give more accurate surface representation, however they cause an increase in the computational cost and complexity. In this chapter, PO results are compared with the integral equation based Method of Moments(MoM) solution. Since PO results agree with the ones in the literature, deviations from MoM solution, which is accepted to be the most accurate, does not mean our approaches give wrong PO results.

3.1 Applications for Plate Structures

This section presents the numerical results of the Physical Optics formulation given in Chapter 2 for plate geometries. Plate sizes used are 1m-1m square, 2m-1m and 4m-1m rectangles. Simulations have been performed for various different initial conditions. Varying parameters are simply, number of facets, incident and observation angles, operating frequency. Simulations are done in such a manner that, one or two variable is fixed whereas another one is changing.

In all cases incident field comes from $+z$ half space and the plate lies on $x-y$ plane. Incident and observation angles are represented by θ and ϕ coordinates in spherical system. Limits for the incident field is $\theta = [0, \frac{\pi}{2}]$ where $\phi = \pi$ and for scattered field $\theta = [0, \frac{\pi}{2}]$ where $\phi = 0$ at this time. Number of facets are changed from 8 to 10.000 in various cases. Simulations are done at frequencies 300MHz, 1.5GHz and 3GHz. Different cases with different angles of incidence and observation are given below.

3.1.1 Case 1: Observation from Specular Direction

In this case, operation frequency is taken as 300MHz. Observation angle and the incident angle is chosen as variables as seen in Figure (3.1). Scattered power is calculated for different number of facets in two different simulations. In figure (3.2) number of facets is 450. Wavelength is 1m which is equal to dimension of the square plate used in this simulation. Therefore, the longest edge of a single facet is $\frac{\sqrt{2}}{15}\lambda$.

In figure (3.2) it is obviously seen that scattered power does not change between approaches, since the main difference between two approaches is in the inclusion of phase in the integration. In figure (3.1), 3 incident and reflected rays are indicated. If we consider the plate as a single facet, there is no phase

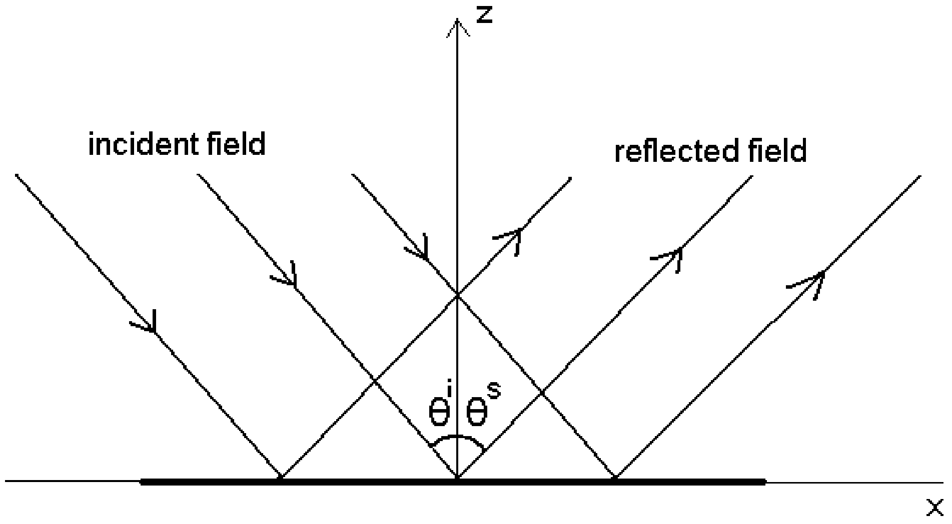

Figure 3.1: Incident and reflected fields for specular observation

difference between these rays since incident and observation angles are equal to each other. Therefore, two approaches give exactly the same results. In figure (3.3), number of facets is increased to 20.000. With the same operating wavelength, ratio between the edge of the triangles and wavelength is $\frac{\sqrt{2}}{100}$.

As depicted in the figures, increasing number of facets changes neither pattern nor maximum scattered power. Additionally, any difference cannot be observed between approaches, therefore it can be concluded that, results for equal incident and observation angles are independent from number of facets. The only point that should be mentioned in these figures is, as the angles get closer to grazing angles, $(\theta, \phi) = (\frac{\pi}{2}, 0)$ and $(\theta, \phi) = (\frac{\pi}{2}, \pi)$, scattered power decreases because cross sectional area of the plate decreases by the cosine of the elevation angle.

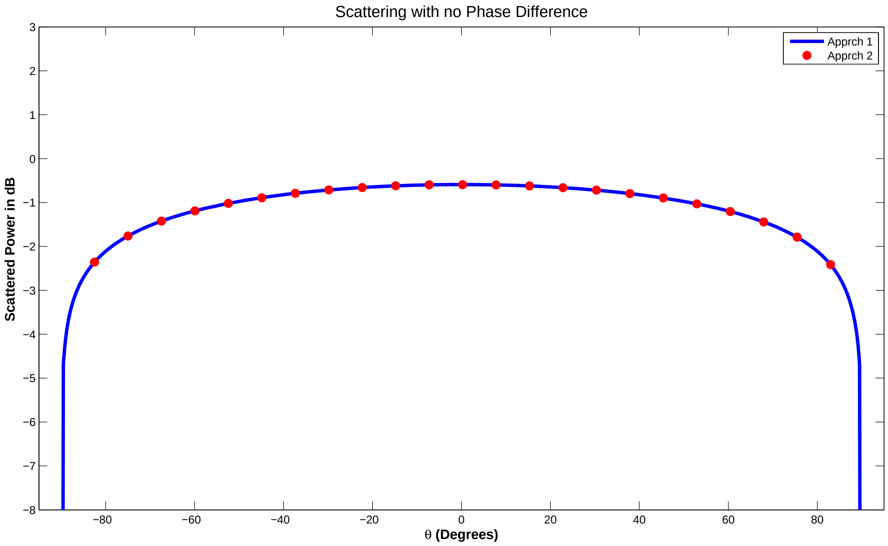

Figure 3.2: Specular observation with 450 facets

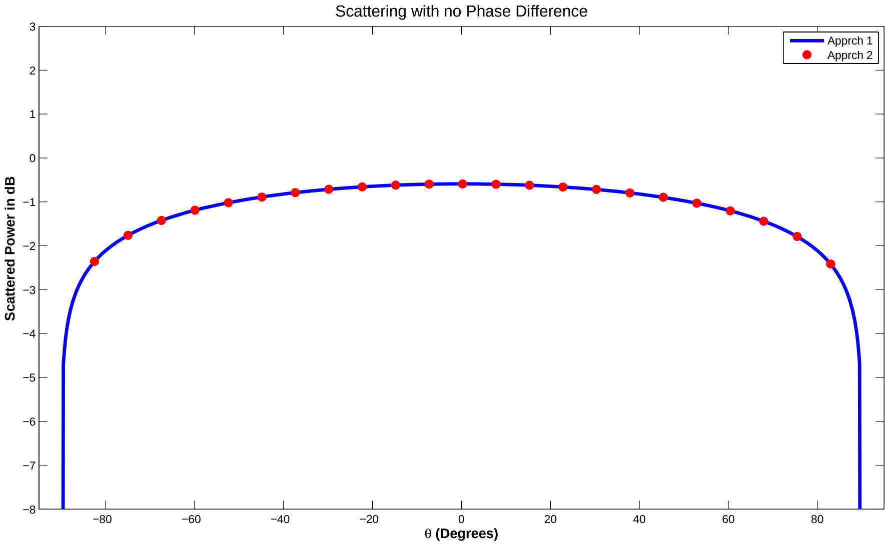

Figure 3.3: Equal incident and observation angles with 20.000 facets

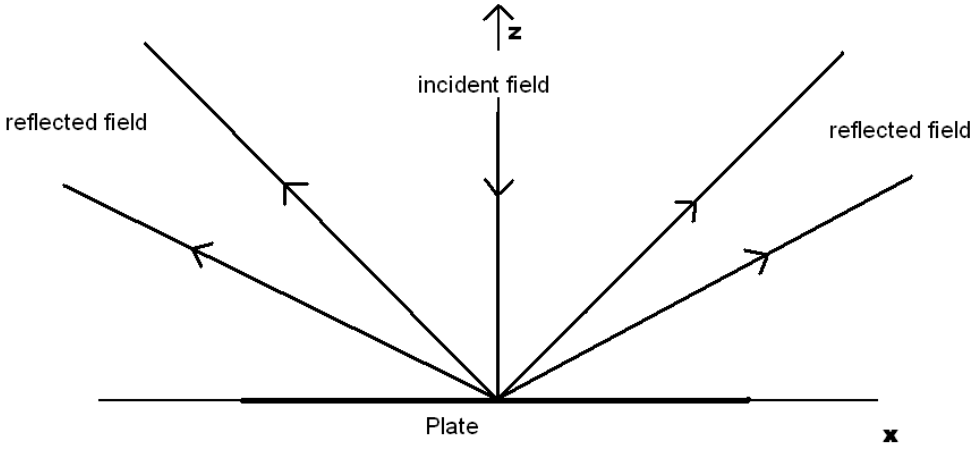

Figure 3.4: Incident and reflected fields for normal incidence - variable observation

3.1.2 Case 2: Normal Incidence - Variable Observation

In this case, the geometry is 1m-1m plate and operation frequency is chosen 1.5GHz. Incident angle is $\theta = 0°$ (normal incidence). Simulations are performed for two different numbers of facets. Figure (3.4) shows the alignment of the plate, incidence and observation.

Greater frequency causes much more phase difference. Therefore, in order to be able to observe the difference between two approaches, frequency is increased to 1.5GHz. In figures (3.5) and (3.6) results of two approaches are shown. Additionally, MoM solution is given in Figure (3.6). [10]

In figure (3.5), number of facets is 8. Increasing the observation angle shall also increase phase difference within a facet, therefore more difference between

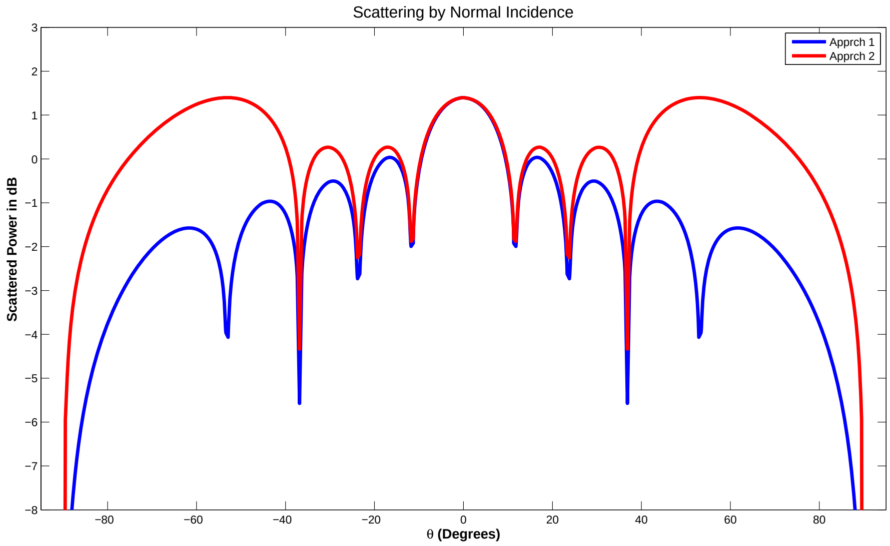

Figure 3.5: Scattered power for normal incidence with 8 Facets

approaches is seen for this case as observation angle gets closer to limit values, $(\theta, \phi) = (\frac{\pi}{2}, 0)$ and $(\theta, \phi) = (\frac{\pi}{2}, \pi)$.

Another point that worth to be mentioned in this figure is, at about $\mp\frac{5\pi}{18}rad$ observation, null points are observed in the results of first approach, however, cannot be seen in the second one. With the second approach, since the phase difference is calculated without any approximation unlike the second technique, some of the null points may be missed due to the roughness of the approximation. This roughness is a function of number of facets, and in figure (3.5), it is seen that 8 facets are insufficient to catch those null points.

In figure, (3.6) number of facets are increased to 2500 and Method of Moments solution is added to the graph. It is obvious from the figure that increasing number of triangles makes the results converge to each other. The first approach, since phase is included in the radiation integral and therefore the results are independent of number of facets, remain unchanged. However, for the other approach, results are highly dependent on how many triangles are used to model the plate, it is observed that increasing number of facets makes the second approach get closer to first one as expected. Third type of line (dashed line) on

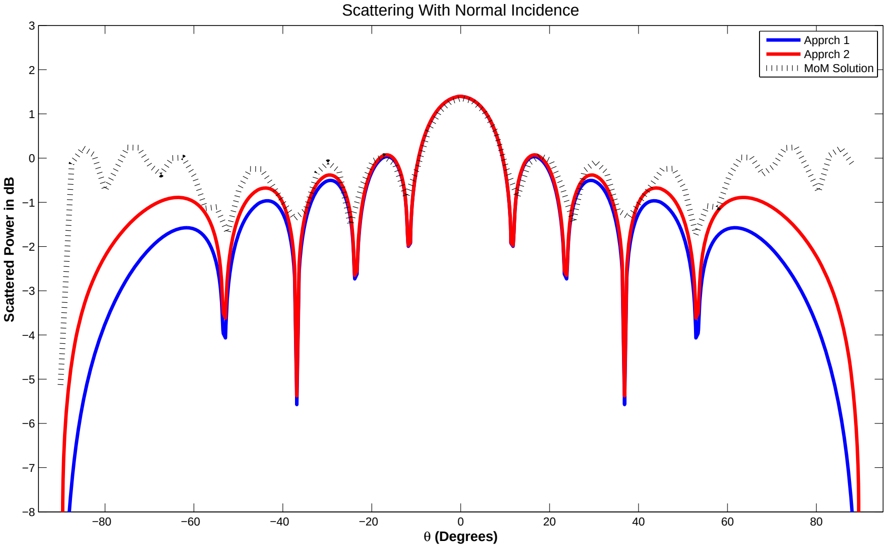

Figure 3.6: Scattered power for normal incidence with 2500 facets including MoM

the figure illustrates Method of Moments solution. For angles around specular point (normal angle for this case) both PO approaches give very good results. However, increasing observation angles causes PO deviates from the Method of Moments solution.

3.1.3 Case 3: Incidence from a Certain Aspect - Variable Observation

In this case, the geometry is 1m-1m plate and the incident angle is $(\theta, \phi) = (\frac{\pi}{6}, \pi)$. Alignment is depicted in figure (3.7). The observation angle varies from $-90°$ to $+90°$ degrees. However at this time, operating frequency is taken as 3GHz. Similar to the previous case, getting away from the GO reflection angle (specular angle, $\frac{\pi}{6}$ in this case), the difference between two approaches appears more. In figure (3.8) number of facets is 512. At the angles less than about $-\frac{\pi}{18} rad$ and greater than about $\frac{2\pi}{9} rad$, two approaches obviously differ, however in figure, (3.9) this difference is smaller since the number of facets is 64 times greater.

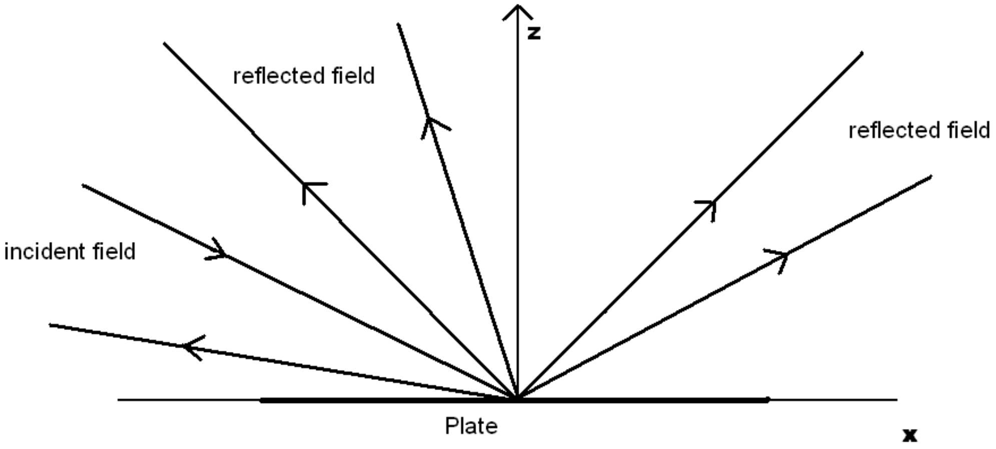

Figure 3.7: Incident and reflected fields for incident from a certain aspect- variable observation

Results for Approach 1 do not change for the two cases since it is independent of the number of facets.

3.1.4 Case 4: Incidence from a Certain Aspect - Variable Frequency

In this case, similar to the simulation in section (3.1.3), the scatterer is a square plate and the incident angle is constant, $(\theta, \phi) = (\frac{\pi}{6}, \pi)$. However unlikely, number of facets is kept constant and equals to 8.192. Operation frequency, on the other hand, changes for each simulation. In figure (3.10) operation frequency is 3GHz. The next two figures, (3.11) and (3.12) are drawn with operation frequencies of 6 GHz and 9GHz, respectively. There are two points to be mentioned:

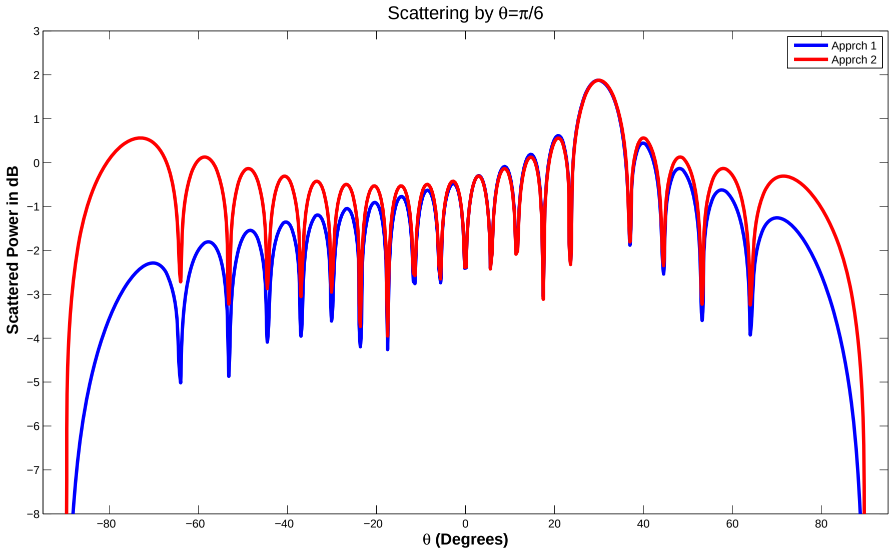

Figure 3.8: Scattered power from $\frac{\pi}{6}$ incidence with facet number of 512

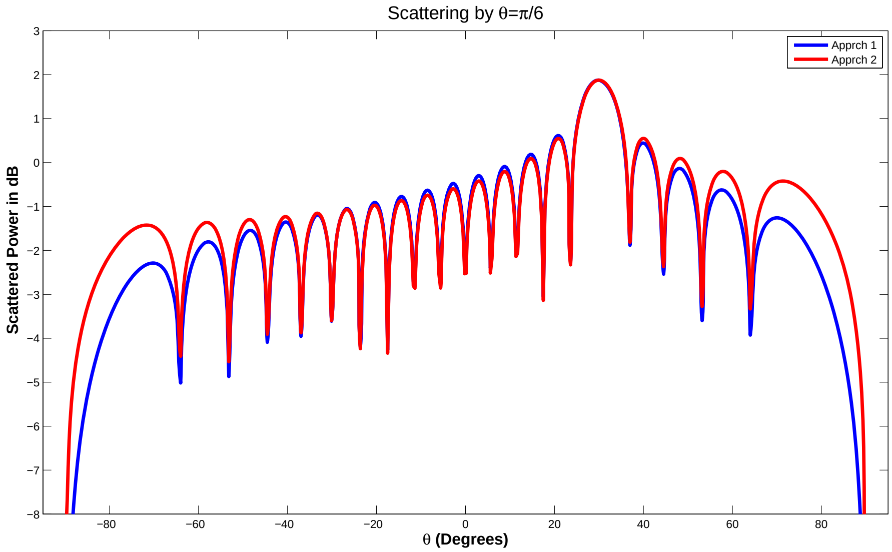

Figure 3.9: Scattered power from $\frac{\pi}{6}$ incidence with facet number of 32.768

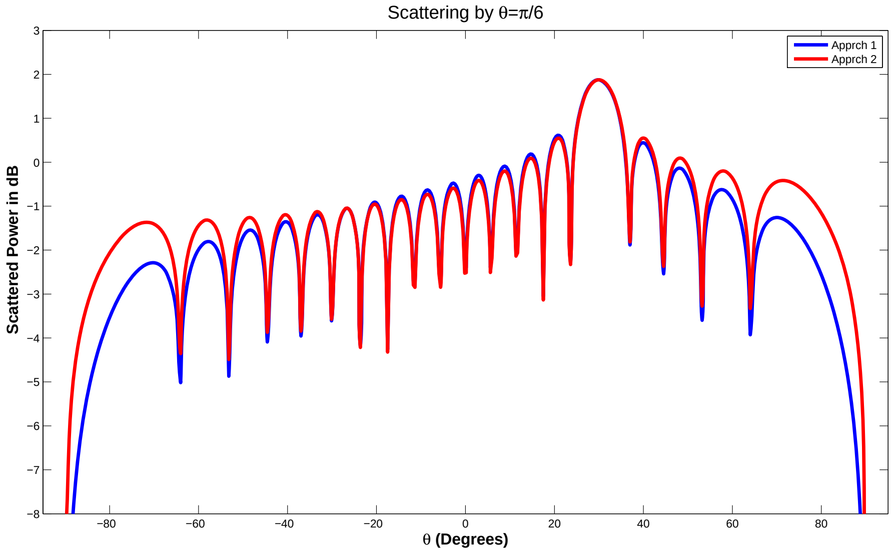

Figure 3.10: Scattered power from $\frac{\pi}{6}$ incidence with frequency of 3 GHz

1. Number of oscillations decreases in the pattern as the frequency decreases. Since higher the frequency make phase change more effectively.
2. Increasing frequency makes the difference between approaches more visible.

3.1.5 Case 5: Evaluation of Approaches with Constant Difference

In order to have a clear idea about the usage of different PO approaches, another type of simulation has been performed. In this case, the square plate is illuminated from different aspects changing between $[0, \frac{\pi}{2}]$. Since it is known that increasing frequency makes the difference between results of two approaches more, the highest frequency is calculated for constant 3 percent difference at the backscattered power. In figure, (3.13) for 4 different facet numbers, simulations are done. For example, for $\theta = 2.88°$ incidence, backscattered power for two approaches is set to 3 percent and maximum frequency value is seeked. This value is about 7.3 GHz for facet number 200, about 14.3 GHz for facet number 800, about 21.4 GHz for 1800 and about 27.3 GHz for facet number 3200.

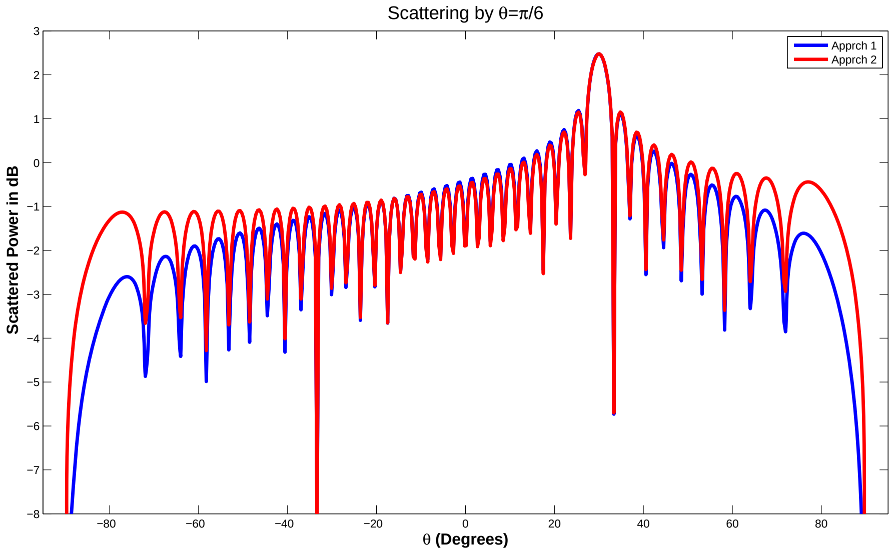

Figure 3.11: Scattered power from $\frac{\pi}{6}$ incidence with frequency of 6 GHz

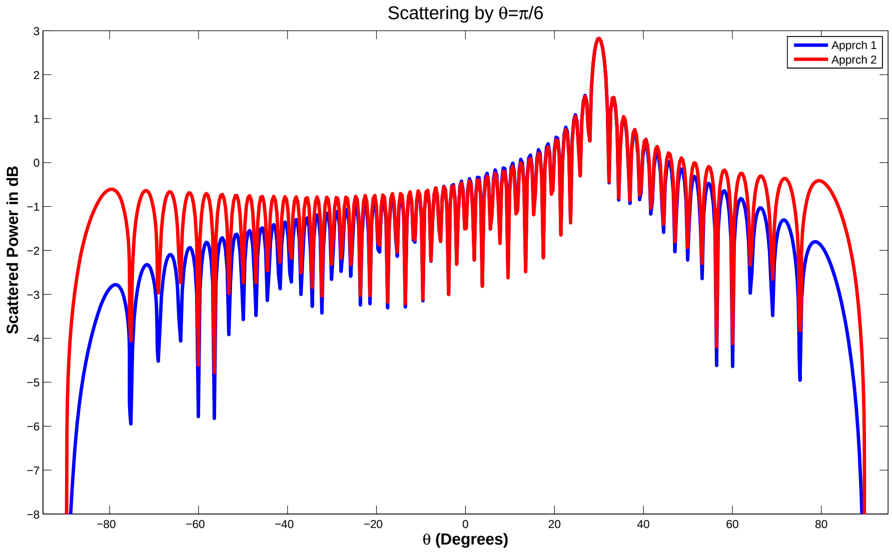

Figure 3.12: Scattered power from $\frac{\pi}{6}$ incidence with frequency of 9 GHz

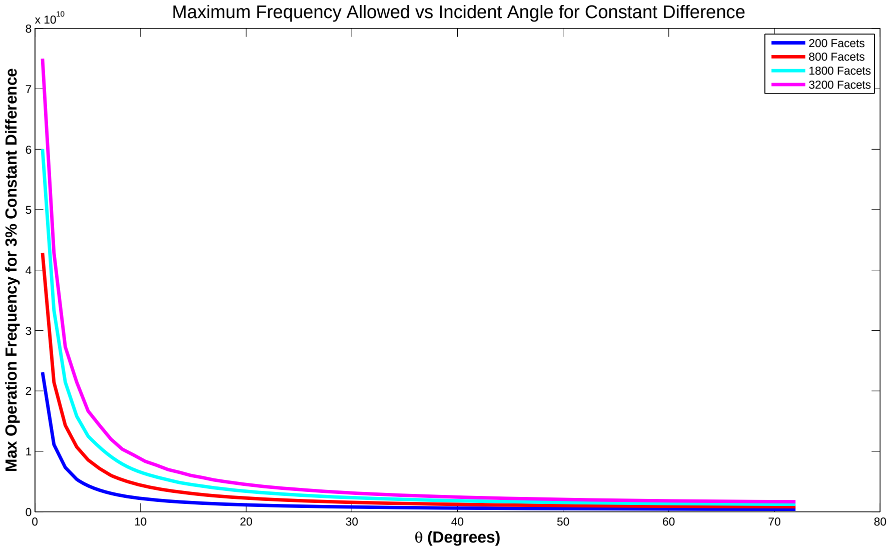

Figure 3.13: Maximum operation frequency for 3 percent constant difference between approaches

Notice that, the ratio between the maximum frequency values that can be used for 3 percent difference and the square root of number of facets appears to be constant. This constant is $\frac{f_{max}}{\sqrt{N}} = 1.66E8$ for $\theta = 9.36°$ and $\frac{f_{max}}{\sqrt{N}} = 5.52E7$ for $\theta = 29.88°$.

Figure (3.13) tells that, increasing number of facets increases the highest frequency for constant 3 percent difference since as the facet number increases two approaches give closer results. On the other hand, getting closer to normal incidence, since phase becomes less effective, frequency limit increases. For normal incidence limit is infinity, as it is depicted in the figure.

3.1.6 Case 6: Applications with Rectangles

In this case, the same simulation geometry is performed in section 3.2.2. The frequency of operation is chosen again 1.5GHz. Incident angle is $\theta = 0°$. Figure (3.4) shows the alignment of the rectangular plate, incident and observation aspects.

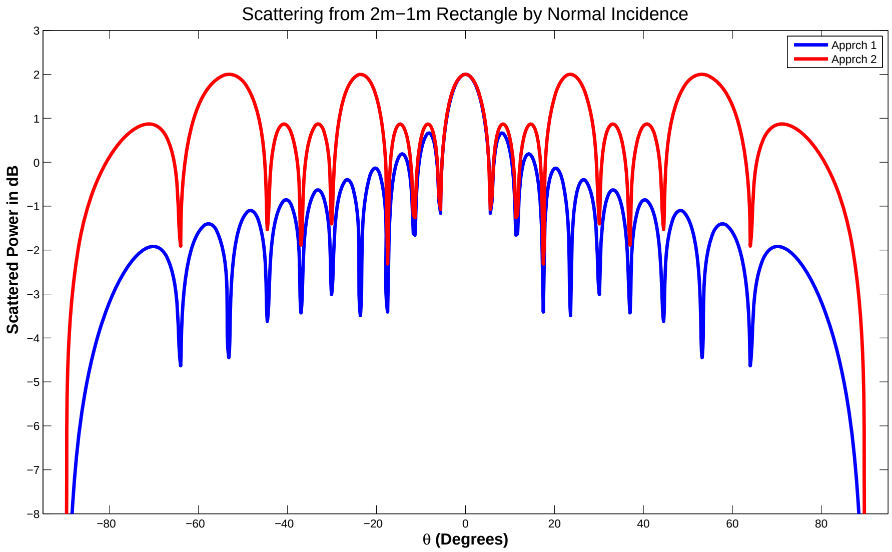

Figure 3.14: Scattered power for normal incidence from 2m-1m rectangle with 8 facets

In figure (3.14), 2m-1m rectangular plate is used. Number of facets is 8 in this simulation. In comparison with figure (3.15), two approaches give closer results to each other due to increased facet number. This number is 128 for the second figure. Similar to Case 2, at some angles, there exist null points that Approach 2 cannot predict. This situation does not exist in the second simulation.

In figures (3.16), (3.17) and (3.18) 1m-1m square plate, 2m-1m rectangular plate and 4m-1m rectangular plate are used for simulations respectively. In these simulations, size of a single facet is the same and equal to $\frac{1}{128}\ m^2$.

In these figures, as one of the dimensions of the plate is increased, the number of oscillations are increased. Actually this result is expected, since increasing the number of facets means there exists more and more field contributions that may affect the total field in a constructive or destructive way.

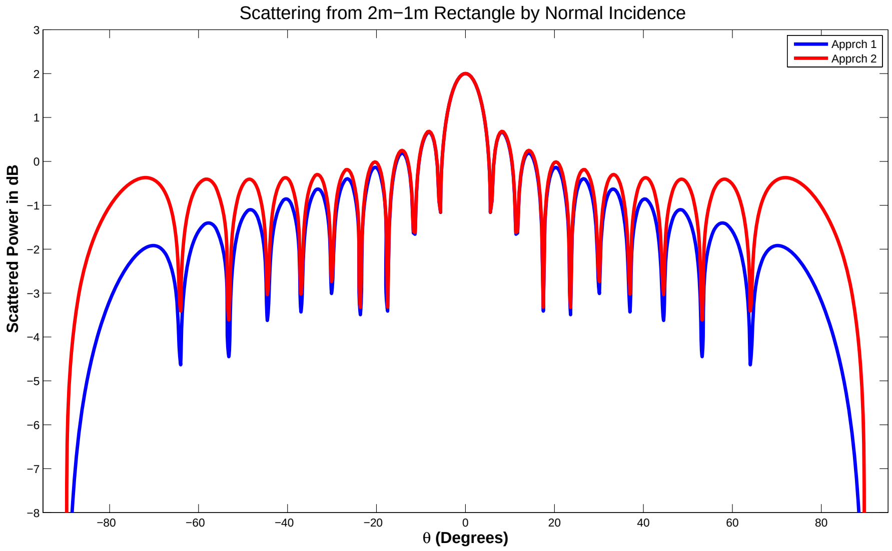

Figure 3.15: Scattered power for normal incidence from 2m-1m rectangle with 128 facets

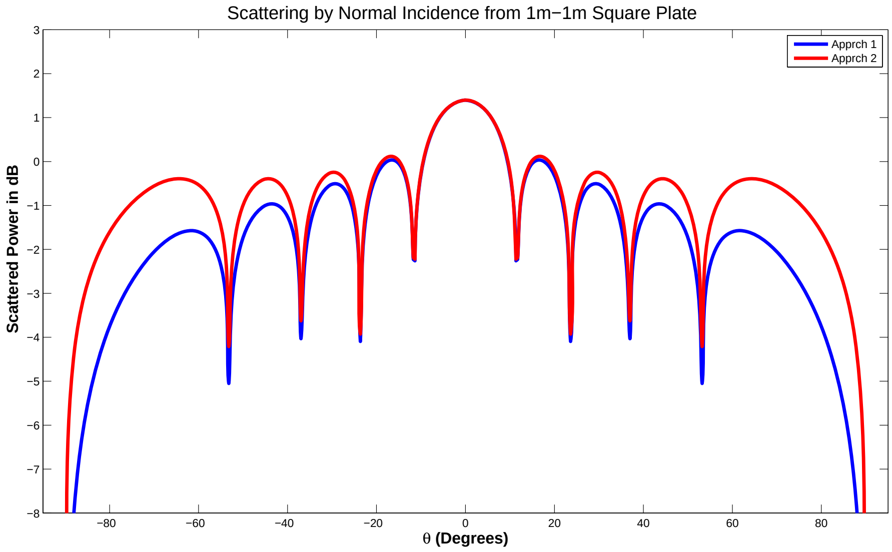

Figure 3.16: Scattered power for normal incidence from 1m-1m square plate with facet size $1/128\ m^2$

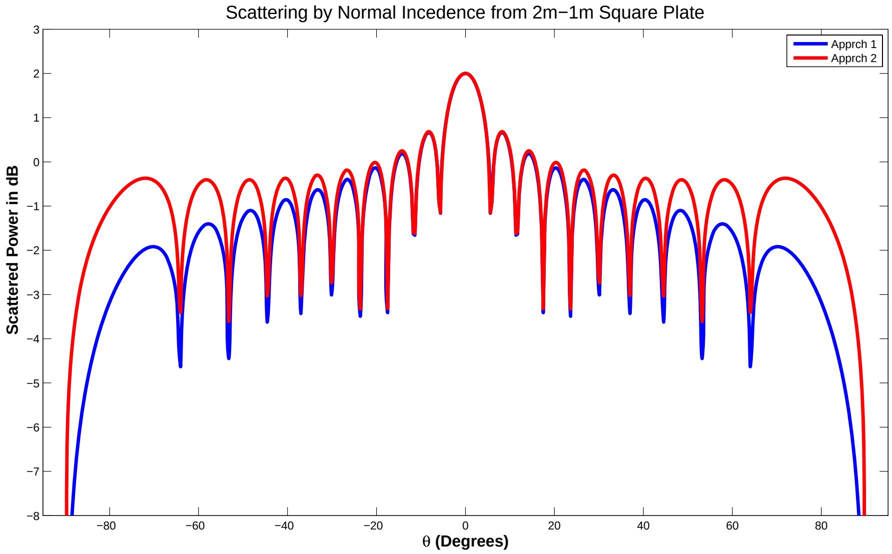

Figure 3.17: Scattered power for normal incidence from 2m-1m rectangular plate with facet size 1/128 m^2

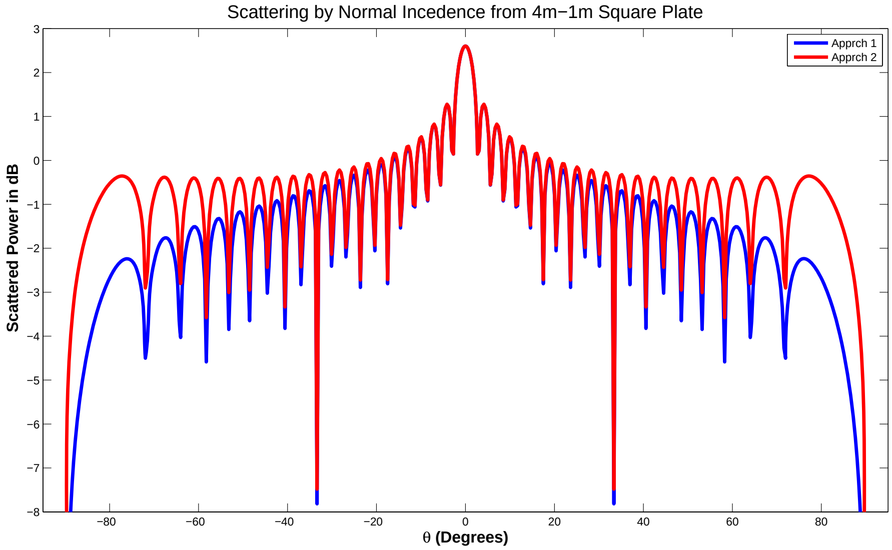

Figure 3.18: Scattered power for normal incidence from 4m-1m rectangular plate with facet size 1/128 m^2

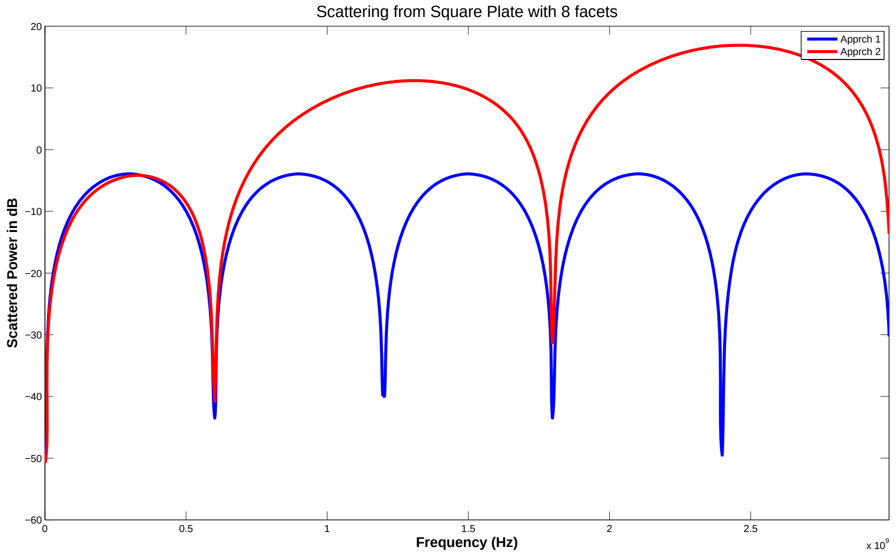

Figure 3.19: Scattered power for normal incidence from square plate with 8 facets varying frequency

3.1.7 Case 7: Frequency Applications with Plates

In this case, the same simulation geometry is performed in figure (3.7). The scatterer is a square plate and the incident angle is $(\theta,\phi)=(\frac{\pi}{3},\pi)$ whereas the observation is the normal direction. At this time, frequency is chosen as the variable.

As it is seen in figures (3.19) and (3.20), scattered power shows an oscillatory behaviour as the frequency increases. Null points occur where the path difference between the incident and observation rays ($\Delta x = a \sin\theta_i$, where a is the edge of the square plate) is an integer multiple of the frequency of operation. As observed, higher frequencies cause two approaches differ from each other as expected. For very low facet numbers, there may be some null points that Approach 2 cannot predict.

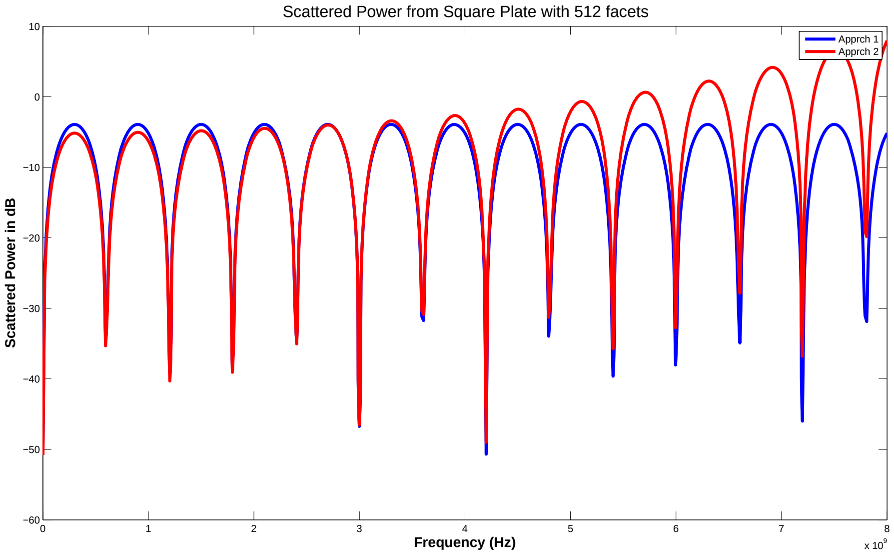

Figure 3.20: Scattered power for normal incidence from square plate with 512 facets varying frequency

3.2 Applications with Spherical Structures

This section presents the numerical results of the Physical Optics formulations given in Chapter 2 for spherical geometries. Simulations have been performed for various different parameters which are simply, number of facets, observation angle, operating frequency, polarizations of incident and reflected waves. Simulations are done in such a manner that, one or two variables are fixed whereas another one is changing.

In all cases, field comes from $+x$ direction. Incident angle may be expressed as $(\theta, \phi) = (\frac{\pi}{2}, 0)$ in spherical coordinates. In the first case, backscattering is considered and frequency varies in order to observe the variation due to the frequency with the two approaches. In the second case, bistatic scattering is discussed. For θ and ϕ polarized incident field, observation angle changes from $\phi = 0°$ to $180°$. The center of the sphere coincides with the origin of the coordinate system. Simulations shall be presented case by case.

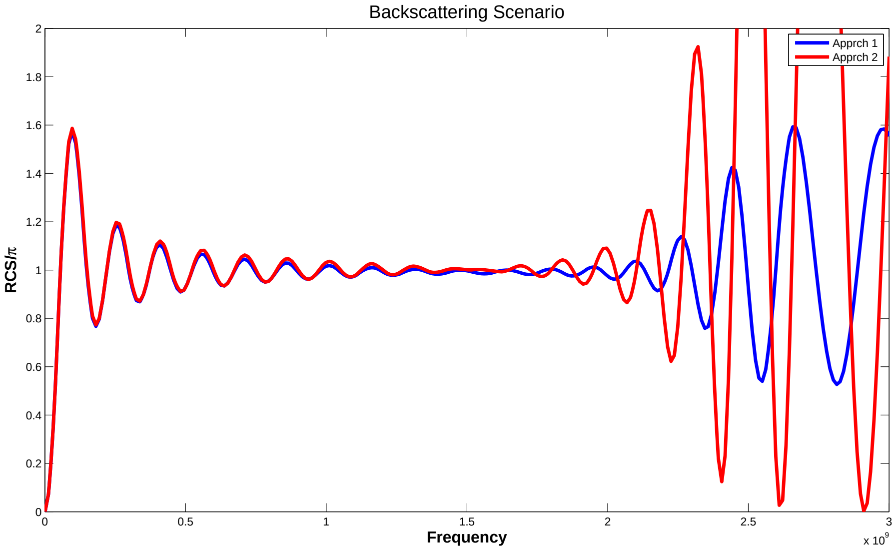

Figure 3.21: Backscattering by ϕ polarized incident wave with facet number of 10.000

3.2.1 Case 1: Backscattering Scenario for Spheres

In this case, the echo area is calculated for a certain frequency band which is chosen differently for various number of facets. In simulations, it is observed that echo area approaches to πr^2 (r is the radius of the sphere) which is the geometrical cross section of the target with increasing frequency. The oscillatory behaviour of the pattern is due to the interaction of PO diffracted and GO reflected field contributions. GO reflected rays correspond to the stationary phase contribution and the PO diffracted field corresponds to the end-point contributions in the asymptotic integration of PO. PO diffracted fields travel an excess path with respect to GO reflected rays. Therefore, peaks occur in the pattern when the path difference is an integer multiple of the wavelength.

In the figures, (3.21), (3.22) and (3.23) number of facets are 10.000, 25.600 and 40.000 respectively. y axis stands for the RCS times $\frac{1}{\pi}$. Since radius is 1m, y axis shall approach to 1.

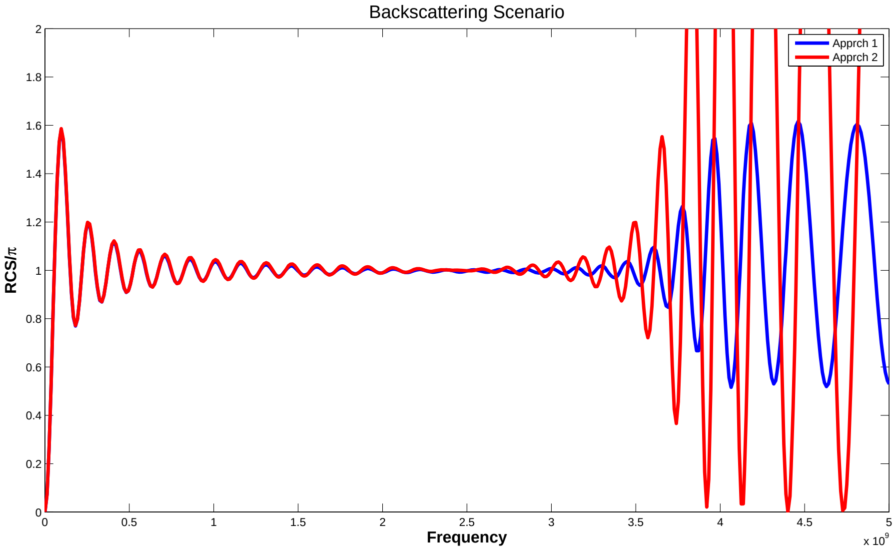

Figure 3.22: Backscattering by ϕ polarized incident wave with facet number of 25.600

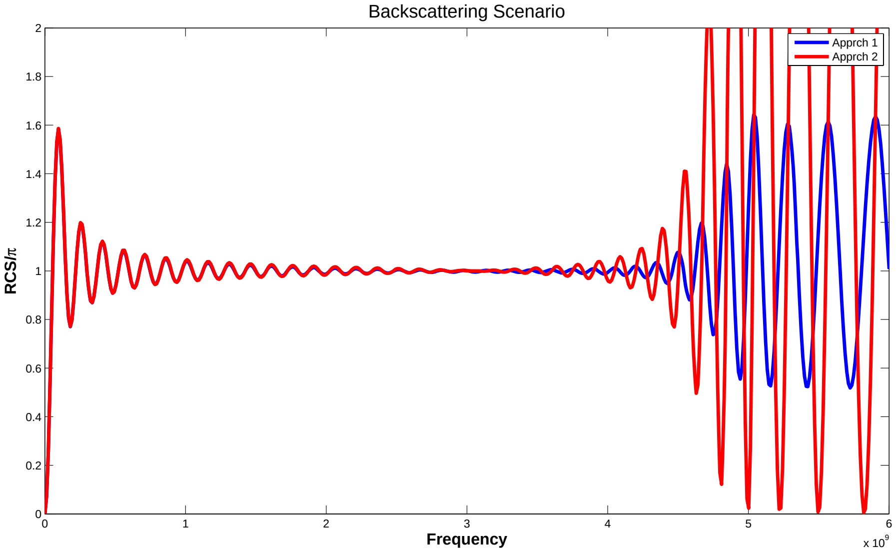

Figure 3.23: Backscattering by ϕ polarized incident wave with facet number of 40.000

In three of the figures, three regions are observed, Low Frequency (Rayleigh) Region, GO Region and let us call the third region as PO diffraction region. In the first region, wavelength of incoming plane wave is quite big with respect to a dimension of the sphere.

Theoretically, echo area of a sphere is its geometrical cross-sectional area for GO, meanly for infinitely high frequencies. The closest results to GO exist in the second region. Here, a critical frequency may be introduced as a boundary value between second and the third region. This critical value, $f_{critical}$, is around 1.5 GHz for number of facets, $N = 10.000$. $f_{critical}$ is about 2.4 GHz for N=25.600. And it is around 3.0 GHz for 40.000 pieces of triangles. As it is seen, ratio between critical frequencies and square root of number of facets is constant, which is $15E6$. Another explanation of this is, edge of a single facet at these critical frequencies is constant and equal to 0.15λ independent of total number of facets. It is going to be investigated that this value is constant for this interval of the number of facets only.

In the third region, results deviate from the Geometrical Optics. The main reason for that is, at very high frequencies, the difference between a perfect sphere and mesh model of it (which is more like a rough sphere or a football) emerges, therefore total field may no longer be calculated accurately. In other words, in order to have good results in PO, lengths of the edges of the facets used in modeling body, should be small in terms of wavelength. For instance, $\frac{\lambda}{10}$ is a de-facto standard in Electromagnetics. Beyond the critical values, this ratio may no longer be prevented, therefore results highly deviates.

However, as depicted in figures, (3.21),(3.22) and (3.23) second approach deviates much faster than first approach. The reason for this is, phase difference is considered to be constant for a single facet and taken the midpoint as reference, as frequency increases error coming from phase calculations becomes considerably high in the contrary of end-point contribution of PO integral. Therefore, total

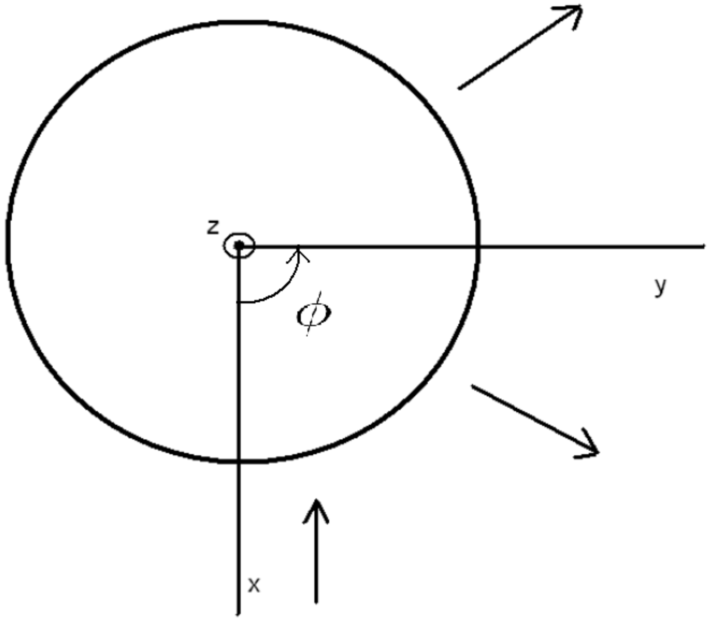

Figure 3.24: Bistatic scenario for scattering from sphere

field calculated with second approach may oscillate with higher amplitudes in comparison with the first approach in the third region.

3.2.2 Case 2: Bistatic Scenario - Different Polarization for Spheres

In this case, incident wave comes from $+x$ direction and observation aspect is chosen such as, $\theta = \pi$ and $\phi = 0$ to π, from backscatter to forward-scatter as shown in the figure (3.24) RCS of the sphere is calculated for two polarizations. There are 6 plots related this case which are $\sigma_{\phi\phi}$ and $\sigma_{\theta\theta}$ vs azimuth angle, ϕ for various different number of facets. Operation frequency is chosen 300 MHz and 900 MHz at this case.

The main point that should be noted at these figures is, as the number of facets are increased two approaches give closer results as expected, since phase calculation is done better and better with second approach.

Another point that is worth to mention is, independent of the approach applied, forward-scattered power is constant for all cases. Actually the reason behind this result is explained in section (3.1.1). Thinking of a single facet, if the observation direction is the specular direction, there exists no phase difference between any two points on the triangle. Therefore, any difference cannot be observed between two approaches. Another case for no phase difference is $\phi_s = \pi - \phi_i$ which is the forward scattering scenario. Therefore, at this aspect angle, two approaches give the same results. Forward-scattered power is also the highest for all angles for all polarizations.

Another noticeable point is, comparing two approaches with Method of Moments Solution , it is obvious that Approach 2 predicts null points better than Approach 1 if there exists a null point. This result is somewhat unexpected, since Approach 2 is an approximated solution whereas Approach 1 is the exact solution of PO radiation integrals. In the figures (3.26),(3.28) and (3.30), around the angle 135°, Approach 2 gives much closer results to MoM solution with respect to Approach 1.

3.2.3 Case 3: Backscattering Scenario for Ellipsoids

In this case, similar to section (3.2.1) Radar Cross Section is calculated for oblate and prolate spheroids. In figure (3.35), setup for this case is illustrated.

For the first two figures, simulations are done for a oblate spheroid. $A = 1m$ is the radius in x and y direction. $B = 0.5m$ is the radius in z direction in this case. In figures (3.36) and (3.37), facet numbers are 2500 and 10.000 respectively. And as expected, boundary frequency values between second and third regions

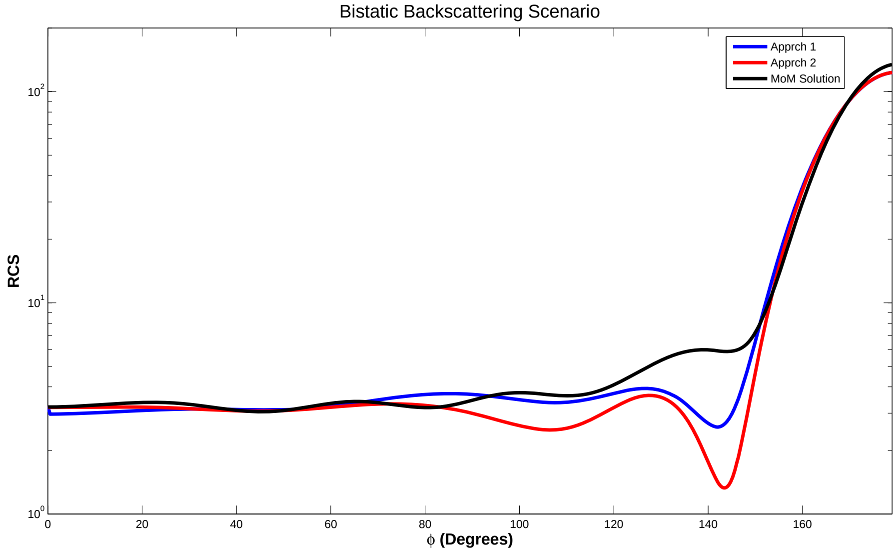

Figure 3.25: Bistatic scenario: ϕ polarized incident wave with facet number of 1024

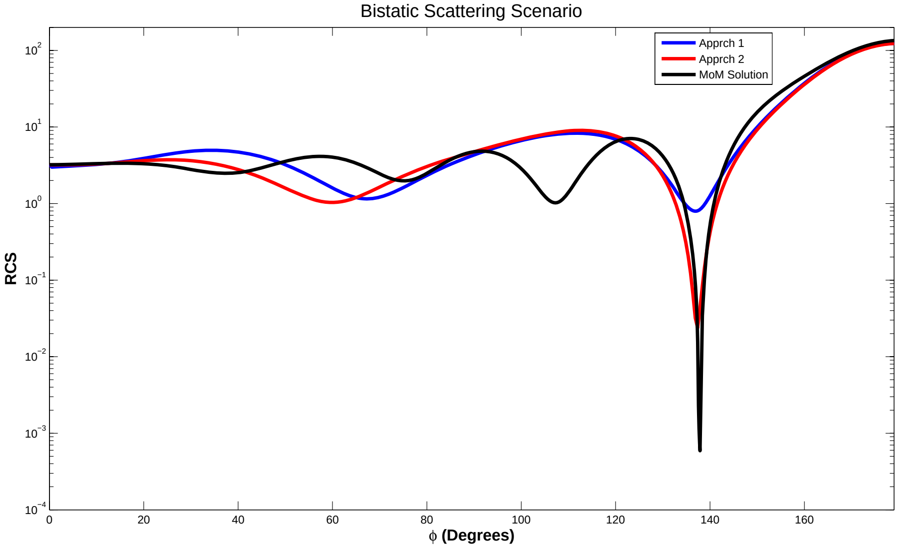

Figure 3.26: Bistatic scenario: θ polarized incident wave with facet number of 1024

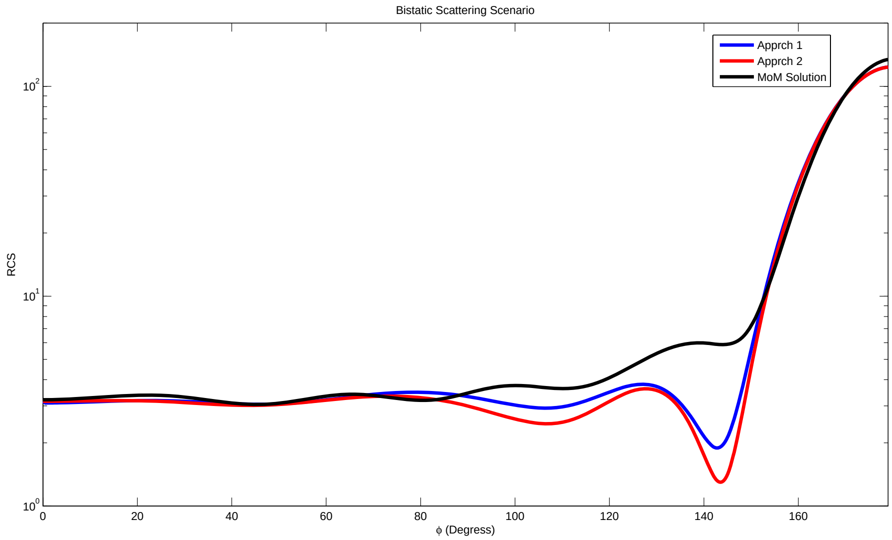

Figure 3.27: Bistatic scenario: ϕ polarized incident wave with facet number of 4096

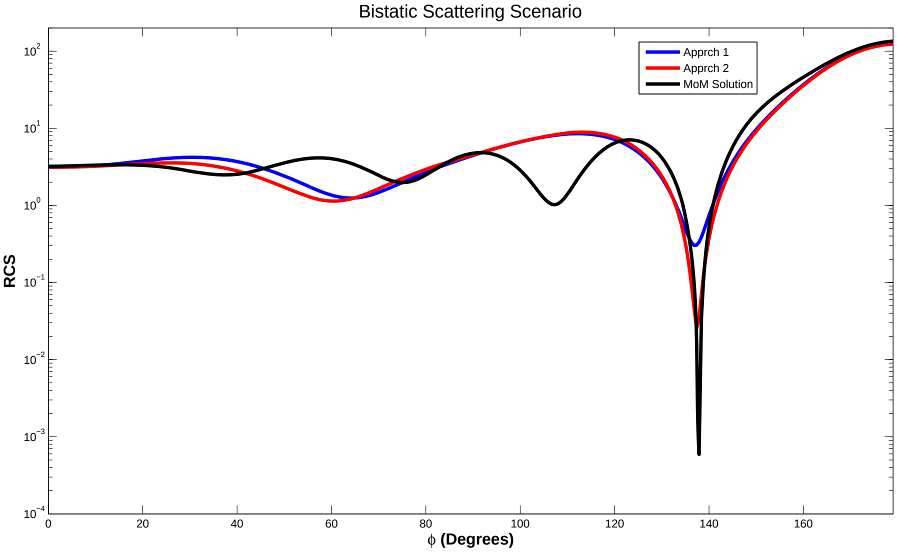

Figure 3.28: Bistatic scenario: θ polarized incident wave with facet number of 4096

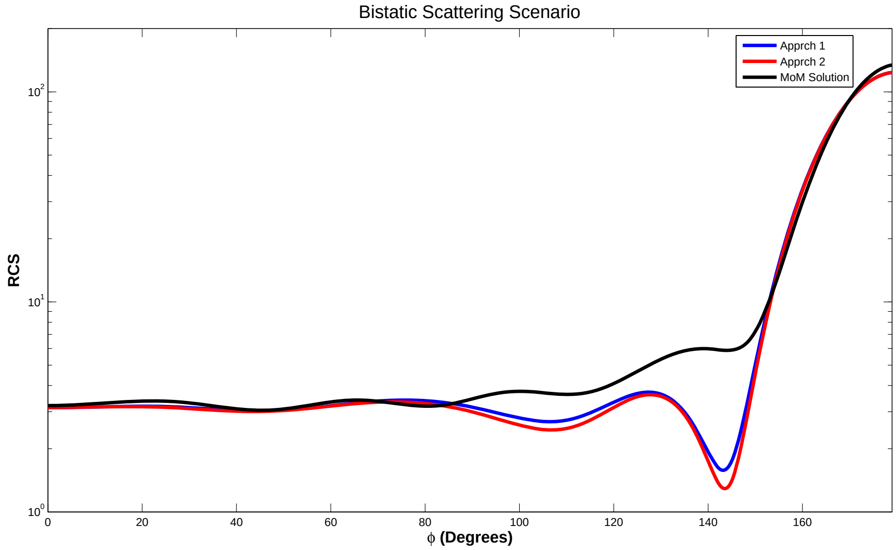

Figure 3.29: Bistatic scenario: ϕ polarized incident wave with facet number of 16384

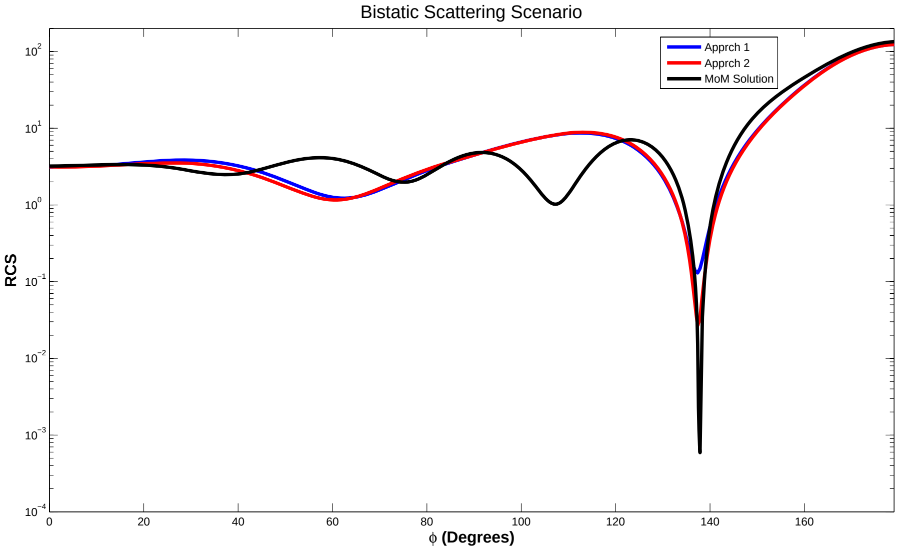

Figure 3.30: Bistatic scenario: θ polarized incident wave with facet number of 16384

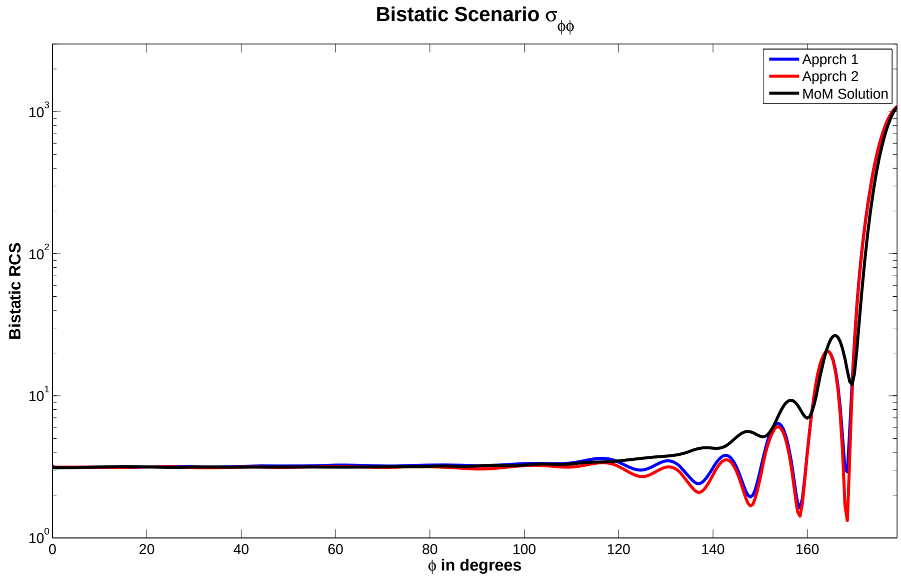

Figure 3.31: Bistatic scenario: ϕ polarized incident wave with facet number of 10.000 at 900MHz

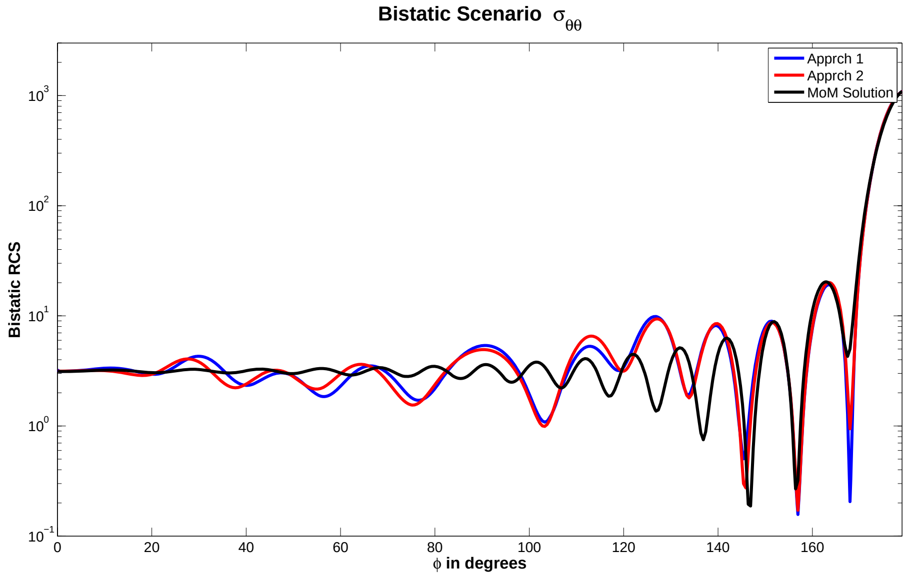

Figure 3.32: Bistatic scenario: θ polarized incident wave with facet number of 10.000 at 900MHz

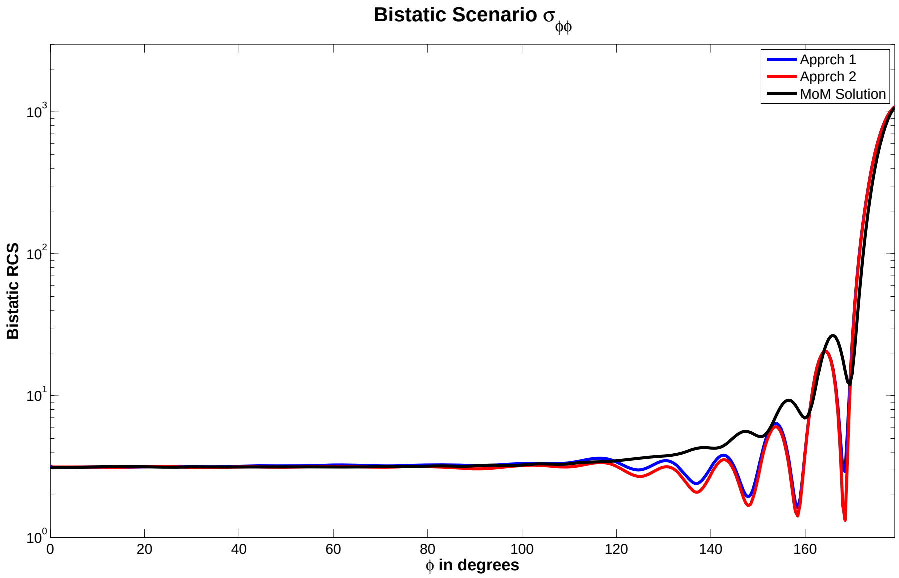

Figure 3.33: Bistatic scenario: ϕ polarized incident wave with facet number of 62.500 at 900MHz

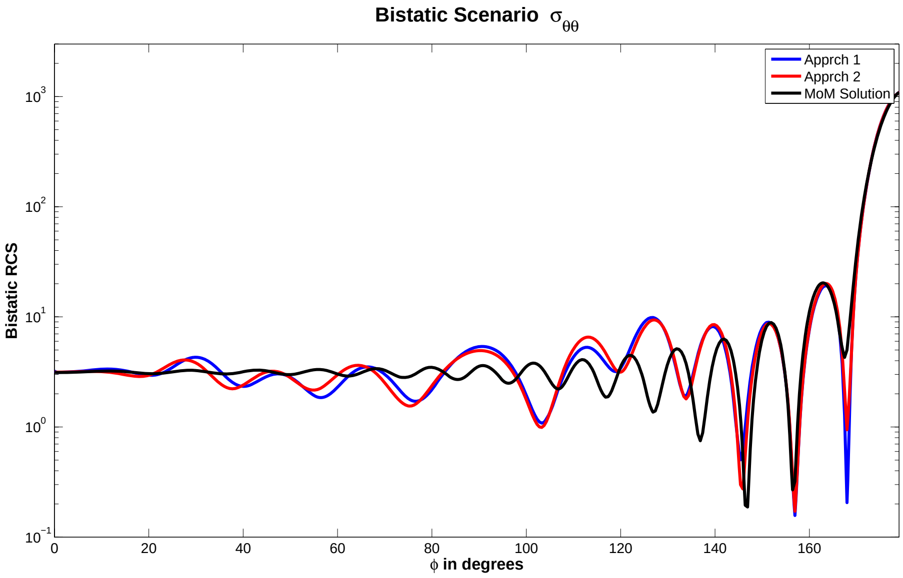

Figure 3.34: Bistatic scenario: θ polarized incident wave with facet number of 62.500 at 900MHz

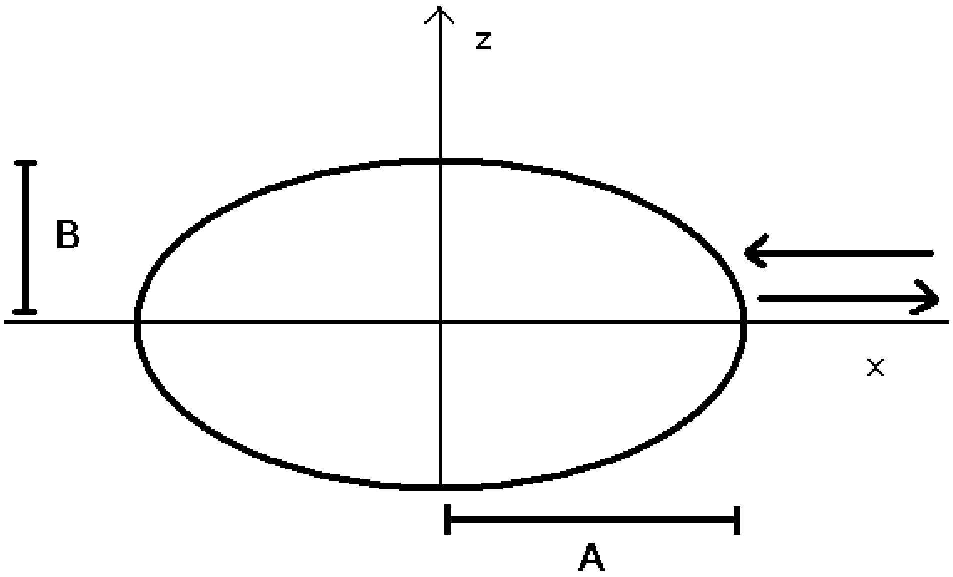

Figure 3.35: Backscattering scenario for scattering from ellipsoid

are increased by number of facets. For sphere case, converged value is the cross sectional area of the sphere, however for this time, results are different. Cross sectional area of an ellipse is given as Area $= \pi AB$. Therefore, area of this oblate spheroid is $\pi AB = 1.570\ m^2$. However, echo area in GO region is even less than 1. Due to GO, reflection depends on the radius of curvature at the specular point. This issue will be investigated thoroughly in another section.

For the prolate spheroid case, $A = 0.5$ is the radius in x axis, $B = 1$ is the radius in y and z axes. The cross sectional area is the same with a unit sphere, however, results in GO region is more than 15. Figures (3.38) and (3.39) show the results of the simulations for this oblate spheroid with 2500 and 10.000 facets respectively.

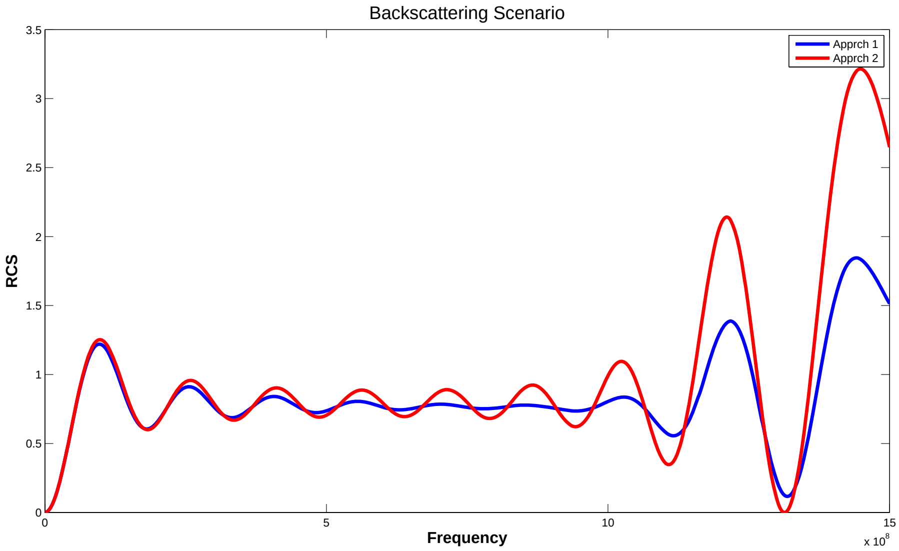

Figure 3.36: Backscattering for a oblate spheroid with A=1m and B=0.5m with facet number 2500

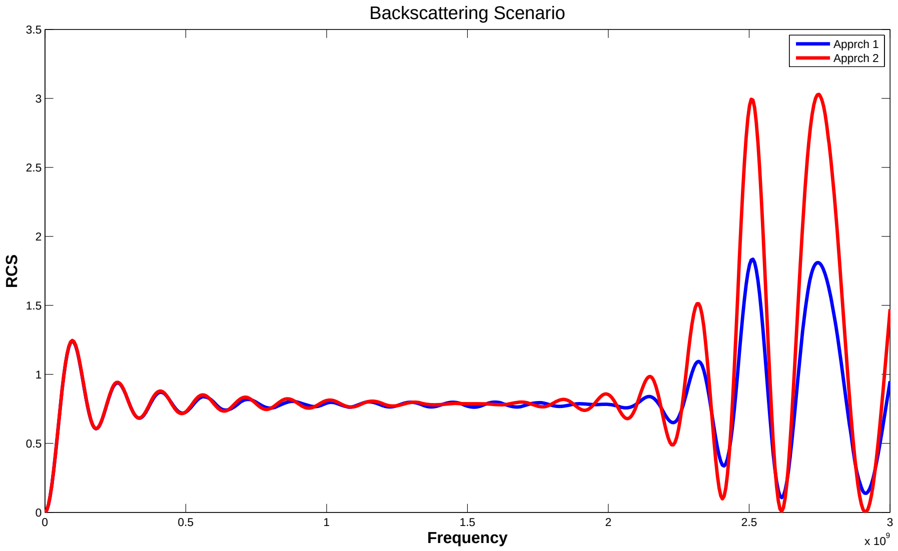

Figure 3.37: Backscattering for a oblate spheroid with A=1m and B=0.5m with facet number 10.000

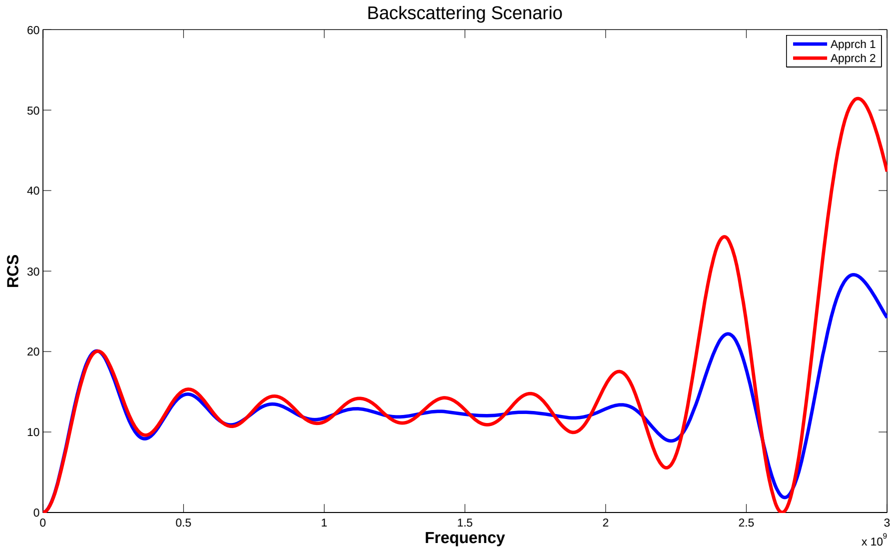

Figure 3.38: Backscattering for a prolate spheroid with A=0.5m and B=1m with facet number 2500

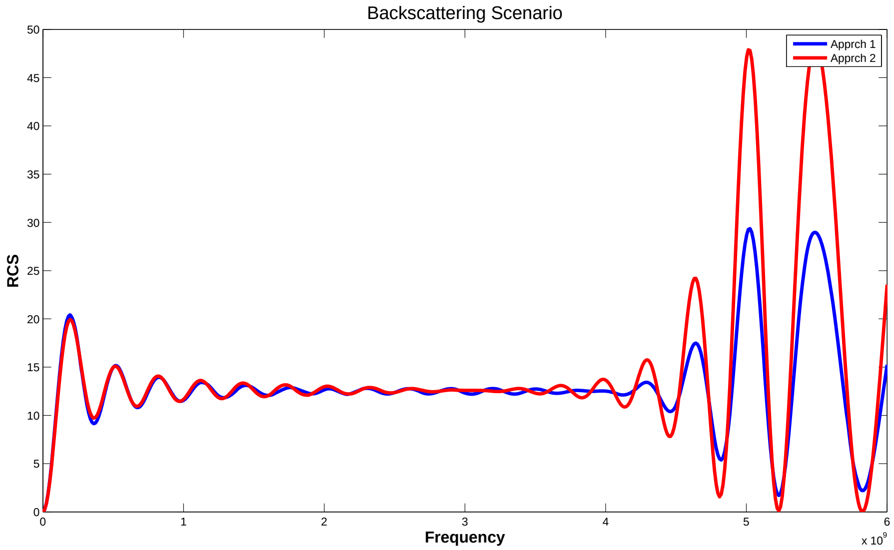

Figure 3.39: Backscattering for a prolate spheroid with A=0.5m and B=1m with facet number 10.000

3.2.4 Case 4: Special Comparison Regarding the Radius of Curvature in GO Calculation

Reflected power in GO depends on the radius of curvature at the specular point. Radius of curvature of a spheroid at the point on the axial direction may be calculated by the following formula [2]:

$$R(u) = -\frac{(B^2 \cos^2 u + A^2 \sin^2 u)^{3/2}}{AB} \tag{3.1}$$

u is the angle between x axis and the line connecting the origin and the point we desire to find the radius of curvature at. A and B are defined in figure (3.35) already. Thinking of a prolate spheroid with radii $A = 1m$ at x axis and $B = 0.5m$ at y and z axes. Incident field is assumed to come from $+x$ direction. Therefore, at specular point, radius of curvature is calculated as $R = \frac{1}{4}\ m$. Due to GO, RCS of a sphere of radius $\frac{1}{4}\ m$ should be equal to this prolate spheroid. For oblate spheroid case, $A = 0.5m$ on x axis and $B = 1m$ for y and z axes. At this time, radius of curvature at the specular point is 2m. Comparisons of these two cases are in figures (3.40), (3.41),(3.42) and (3.43). Number of facets is 10.000 for all simulations at this section.

As seen in figures, our calculations are consistent with the GO. However, the critical frequency value changes between spheres and ellipsoids having the same radius of curvature. For instance, the critical value for the oblate spheroid (Figure (3.40)) is about 2GHz, whereas the same value (Figure(3.41)) is about 8GHz for the sphere which has the same radius of curvature. Similarly, critical frequency value in figure (3.42) is about four times greater than that value in (3.43). Since that critical frequency depends on the size of a facet and for all these simulations, total number of facets is constant, the sphere or ellipsoid which is smaller, namely the ones whose facets are smaller, has this value much less than the other. In figure (3.44), a simulation is performed using a sphere with radius

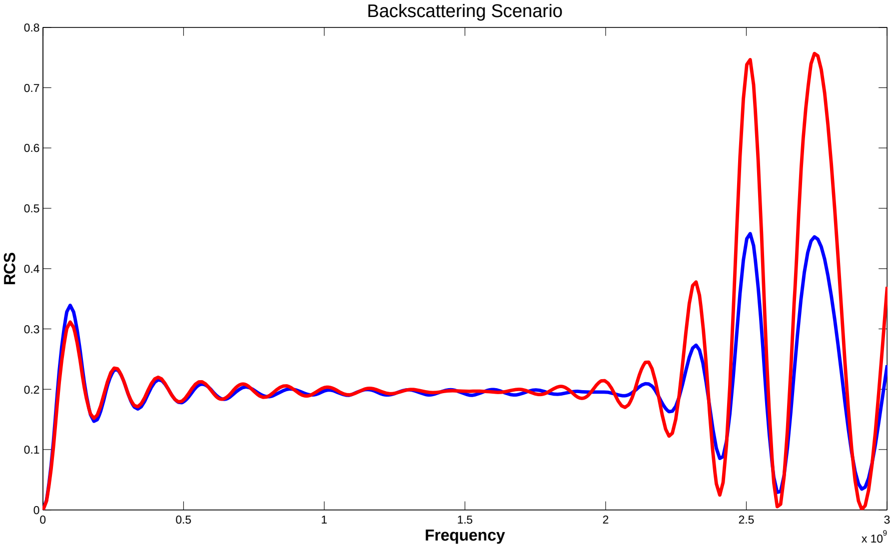

Figure 3.40: Backscattering for a oblate spheroid with A=1m and B=0.5m

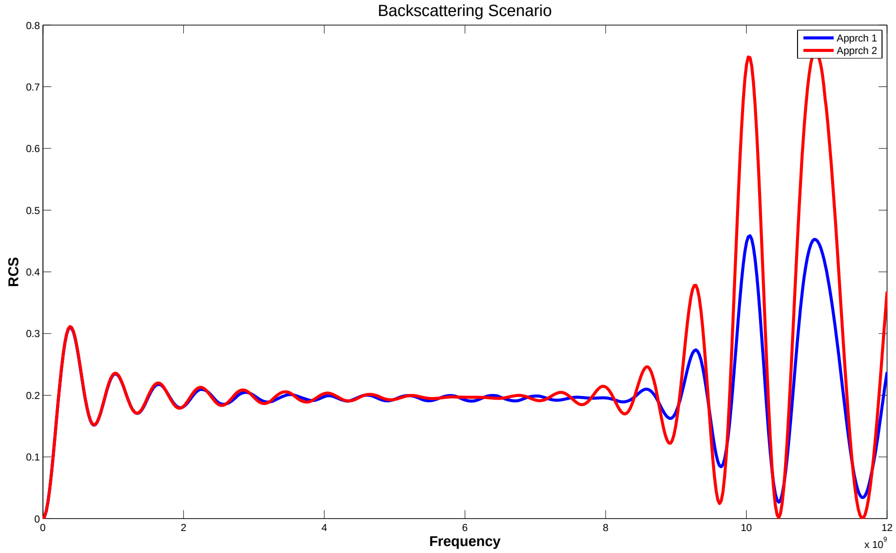

Figure 3.41: Backscattering for a sphere with radius R=1/4

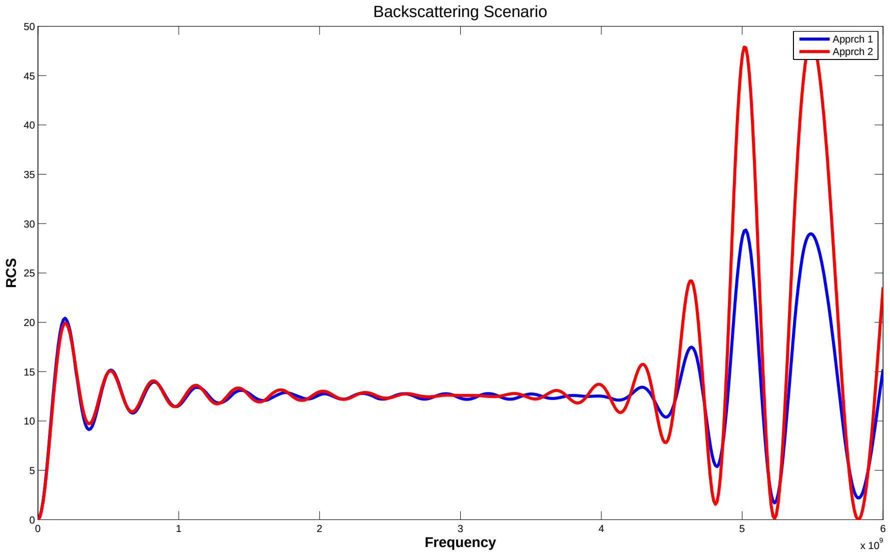

Figure 3.42: Backscattering for a prolate spheroid with A=0.5m and B=1m

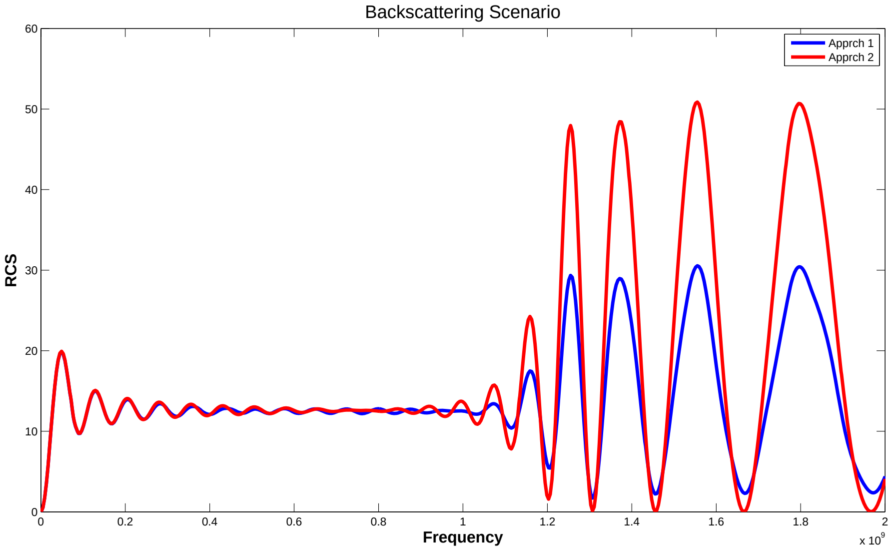

Figure 3.43: Backscattering for a sphere with radius R=2

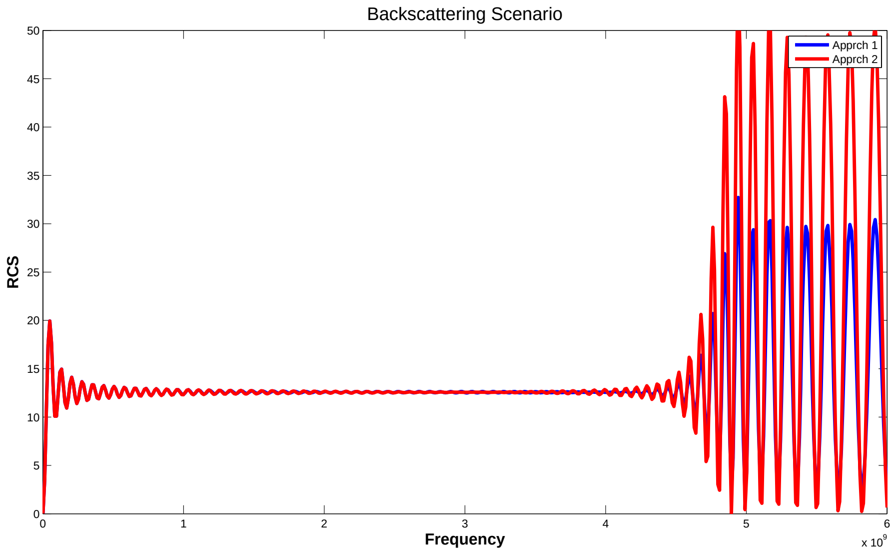

Figure 3.44: Backscattering for a sphere with radius R=2 with excess facets

of 2m as in figure (3.43). At this time, dimension of a single facet is the same as the prolate spheroid in figure (3.42). It is observed that critical frequency value is the same.

3.2.5 Case 5: Usability Analysis of PO Approaches

In this case, a series of simulations are performed in order to obtain an idea about modeling curved surfaces and application of the PO. Since curved surfaces are modeled with planar triangular facets, they are actually not curved surfaces in the simulations any more (ie. a perfect sphere or a football). Using large number of facets and small operation frequencies, the difference between a sphere and a football may be invisible for our calculations. However, as the frequency increases, these differences become more and more visible and cause the results deviate from the theoretical GO, ie RCS of a sphere is its cross sectional area in high frequency region.

The critical frequency that the deviation begins is clearly a function of dimension of the facets used in modeling. In this case, these critical frequency values

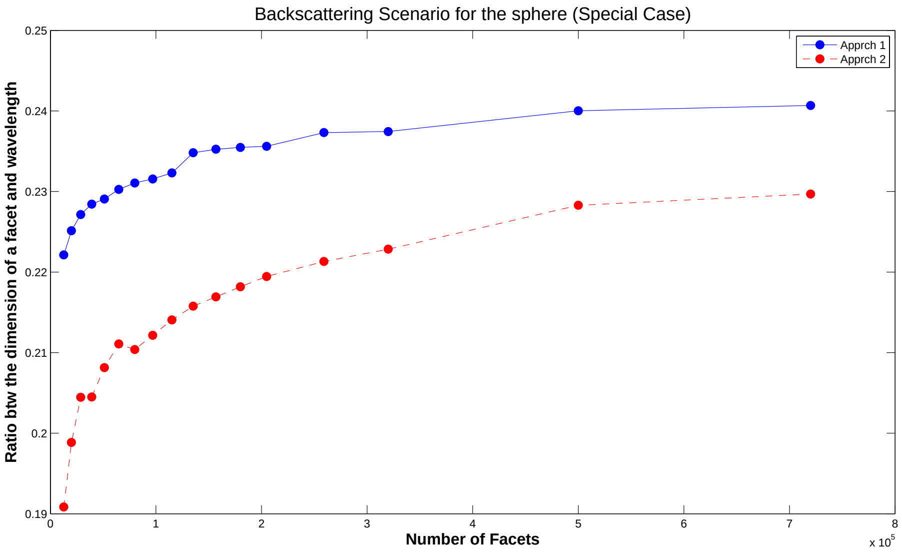

Figure 3.45: Number of facets vs dimension of a facet at the critical frequency

are recorded and plotted with respect to the dimension of a facet. In defining the values, 5 percent deviation is taken as the criteria. Also, a plot is generated in which one has the opportunity to compare the ratio between the dimension of a facet and the operation wavelength versus the total number of facets.

It is seen in figures (3.45) and (3.46), the dependence of accuracy of the approaches to the dimension of a single facet is not linear as expected. Increasing the number of facets, the model gets better, faster than the speed of dimension's getting smaller.

A similar simulation is performed in order to link the radius of curvature to the critical frequency. In figure (3.47), it is seen that for constant number of facets (10.000 in this case) increasing the radius decreases the critical frequency. However, for small values, a unit decrease in curvature effects this limit more than for respectively large values. This result is consistent with the previous ones. Since the radius increases as the total number of facets is fixed, modelling accuracy decreases.

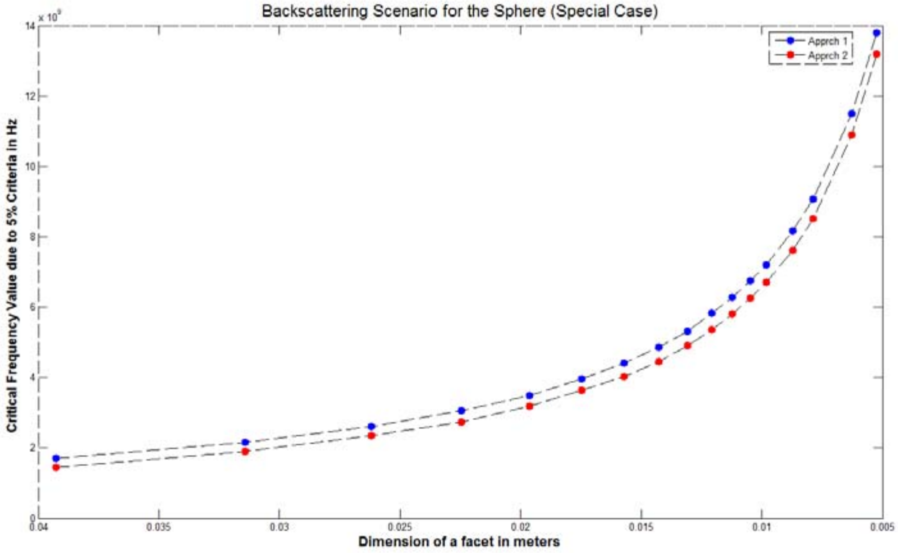

Figure 3.46: Dimension of facet vs critical frequency

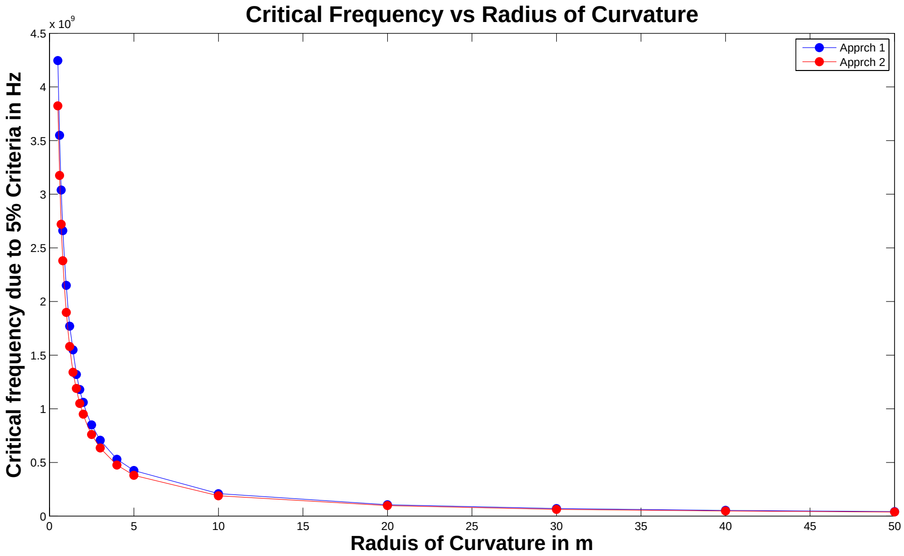

Figure 3.47: Radius of curvature for constant facet number vs critical frequency

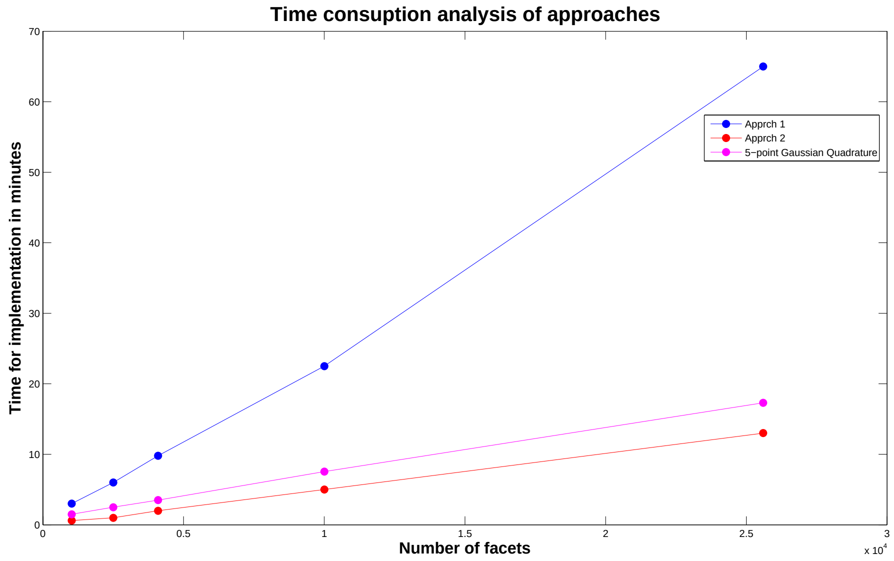

Figure 3.48: Time consumption of approaches

3.2.6 Case 6: Time Consumption Analysis of Approaches

In this case, time consumption analysis is done for two approaches and another technique for numerical integration which is called, Gaussian quadrature. 5-point Gaussian is used in the simulations. As seen in figure (3.48), time consumed by Approach 1 is quite larger than Approach 2 whereas the accuracy is not that much better. On the other hand, Gaussian quadrature method takes acceptable time, however results are less precise than both approaches.

Chapter 4

CONCLUSIONS

In this work, a computer program which uses Physical Optics (PO) method to calculate the RCS of perfectly conducting planar and spherical structures is developed. MATLAB is used as the high-level computing tool. The target bodies are modeled with triangular meshes. The program includes a mesh generation algorithm.

PO which is one of the high frequency techniques, approximates the induced surface currents predicted by GO and integrates them over the surface in order to calculate total scattered field. Two approaches are introduced in this work for calculating this radiation surface integral.

In the first approach, the PO integral is calculated analytically and this analytical solution is used. However, for curved surfaces, using large pieces damages the modeling accuracy; therefore results may differ widely from exact solutions. On the other hand, applying analytical solution instead of taking the integral directly lessens the computational cost and makes the computation much faster than Method of Moments solution.

However, there exists another approach which has much less computation cost than the previous one. In this second approach, phase difference within a facet is assumed to be constant. Namely, a single facet has an area but is considered as a point in phase calculation point of view. However by this way, the accuracy of this approach becomes dependant on the size of the meshes. Larger meshes deviate the result from both results of first approach and from Method of Moments solution.

In this study, a comprehensive comparison has been carried out for several conditions. For plate geometries, for the case the observation is the specular direction, since phase is not an issue within a facet, two approaches does not differ. Similarly, since spheres are modeled using flat facets, forward scattering power is independent of PO integral approach.

For all simulations, the unchanged truth is that, increasing the number of facets two approaches put closer results out. This fact is independent from geometry, frequency of operation or any other variable. On the other hand, results of Approach 1 are independent of number of facets used in modeling for plate geometries but dependent for spheres. For a certain frequency, more deviation from specular aspect makes results of the approaches more apart. This is because the phase difference between any two facets and within a facet gets more.

For plate geometries (squares and rectangles), for fixed difference between results at a particular aspect angle (backscattering aspect), maximum operation frequency increases by number of facets and by incident angle (getting closer to normal incidence). This is because the phase difference lessens.

For rectangles, keeping the facet size constant, increasing one dimension of the plate causes more oscillations which is expected due to increase in the number of reflectors (facets). A simulation for certain and different incident and observation angles and varying frequency is performed. It is observed that, all null points in the results of both approaches coincide. Due to interference, scattered power shows an oscillatory behavior and as the frequency increases two approaches differ from each other for a certain number of facets.

For spheres, backscattering and bistatic scattering scenarios have been performed. For backscattering case, frequency is the variable for each simulation. For very high frequencies, PO gives erroneous results because asymptotic approximation fails since ratio between an edge of a facet and wavelength exceeds a limit. In the simulations, this limit is designated as a function of dimension of facets. Namely, as the frequency gets higher and higher, difference between a perfect sphere and a meshed model becomes observable.

Simulations for ellipsoids are performed for oblate and prolate spheroids. According to the GO, RCS of a scatterer is a function of the radius of curvature at the specular point. In this case, oblate and prolate spheroids are compared with the spheres having the same radius of curvature and facet number. It is shown that our implementation is true for backscattering case. Also, regarding the critical frequency value, (the boundary value between GO and PO diffraction regions, see section 3.2.1) a sphere of the same radius of curvature with the spheroid and the dimension of a facet, is compared and observed that this critical value is a function of dimension of the facets used in modeling. This function is tried to be determined by a simple application. The frequency values at which the results deviate from the GO for a certain amount are recorded. It is observed that, critical frequency is inversely proportional with the square of dimension of the facet.

To conclude, the PO is computationally very advantageous in comparison with the Method of Moments and it gives very good results around specular direction. Among these approaches, for flat surfaces, Approach 1 is better. Because, in order to have close results, Approach 2 needs very large number of facets so much computational cost. However, for curved surfaces, Approach 2, since it gives quite good results in about one fourth of the time spent by Approach 1, is preferable.

Bibliography

[1] R. Harrington, "Time-Harmonic Electromagnetic Fields," *McGraw-Hill*, vol. 33, p. 34, 1961.

[2] D. McNamara, C. Pistorius, and J. Malherbe, *Introduction to the uniform geometrical theory of diffraction.* Artech House Boston, 1990.

[3] P. Pathak, "Techniques for high frequency problems," *Antenna Handbook*, pp. 96–115, 1988.

[4] W. Gordon, "High frequency approximations to the physical optics scatteringintegral," *Antennas and Propagation, IEEE Transactions on*, vol. 42, no. 3, pp. 427–432, 1994.

[5] V. Stein, "Application of Equivalent Edge Currents to Correct the Backscattered Physical Optics Field of Flat Plates," *Applied Computational Electromagnetics Society Journal*, vol. 7.

[6] R. Ross, "Radar cross section of rectangular flat plates as a function of aspect angle," *Antennas and Propagation, IEEE Transactions on [legacy, pre-1988]*, vol. 14, no. 3, pp. 329–335, 1966.

[7] C. Balanis, *Antenna theory.* Wiley New York, 1997.

[8] E. Knott, M. Tuley, and J. Shaeffer, "Radar Cross Section," 2003.

[9] J. Richmond, "A COMPUTER PROGRAM FOR PHYSICAL-OPTICS SCATTERING BY CONVEX CONDUCTING TARGETS.," 1968.

[10] B. Tiryaki, “Solution with method of moments,” *Personal Communication*, 2008.